

Langmuir and upper hybrid waves in Earth's magnetotail

D. B. Graham¹, Yu. V. Khotyaintsev¹, M. Andre¹

¹Swedish Institute of Space Physics, Uppsala, Sweden.

Key Points:

- 1: Intense Langmuir and upper hybrid waves are observed in Earth's magnetotail.
- 2: Langmuir waves are primarily generated by electron beams in the plasma sheet boundary layer.
- 3: Upper hybrid waves are typically associated with beams or loss-cone-like distributions in the plasma sheet boundary layer.

Abstract

Waves at the electron plasma frequency are found throughout the heliosphere. They provide indicators of unstable electron distributions, are routinely used to estimate the local electron number density, and can lead to radio wave emission at the plasma frequency and its harmonics. Although they have been studied extensively in various solar and heliospheric plasma regions, there is a lack of statistical studies of plasma frequency waves in Earth's magnetotail. Here, the occurrence and properties of plasma frequency waves, namely Langmuir and upper hybrid waves, are investigated in Earth's magnetotail using the four Magnetospheric Multiscale spacecraft. In Earth's magnetotail plasma frequency waves are observed about 1 % of the time. About 80 % of the waves are identified as Langmuir waves, while about 20 % are identified as upper hybrid waves. The waves are primarily found in the plasma sheet boundary layer. By comparing with the local electron distributions it is shown that the Langmuir waves are generated by the bump-on-tail instability, while upper hybrid waves are typically associated with broad electron beams or loss-cone-like distributions. The majority of the waves are found in close proximity to ion outflow regions associated with magnetic reconnection in the magnetotail. The waves are likely generated by plasma sheet electrons escaping along newly reconnected magnetic field lines or electron beams propagating toward the distant magnetotail.

1 Introduction

Waves at the electron plasma frequency, namely Langmuir and upper hybrid (UH) waves, are ubiquitous in plasmas and have been observed in almost all regions explored by spacecraft (Briand, 2015). Langmuir waves are narrowband quasi-electrostatic waves with electric field fluctuations that are closely aligned with the background magnetic field. UH waves are quasi-electrostatic waves with electric field fluctuations perpendicular to the background magnetic field. Langmuir waves are well known to be generated by the bump-on-tail (beam-plasma) instability (Scarf et al., 1971), while UH waves can be generated by electron beams, loss cone, shell, or ring distributions (Tataronis & Crawford, 1970; Winglee & Dulk, 1986; Wong et al., 1988). In the near-Earth plasma environment, Langmuir and/or UH waves are routinely observed in Earth's electron foreshock (Etcheto & Faucheux, 1984; Filbert & Kellogg, 1979), at the magnetopause and in the magnetosphere (Graham et al., 2018), at the plasmopause (Kurth et al., 1979), and in the auroral regions (McFadden et al., 1986).

Langmuir and UH waves are important for understanding the local plasma conditions. Nonthermal waves provide an indicator of unstable electron distributions in the plasma. Langmuir and UH waves are important sources of radio emission at the fundamental and harmonics of the local plasma or upper hybrid frequency, and lead to radio remotely observed radio waves, such as from type II and type III radio bursts (Cane et al., 1982; Lin et al., 1981), and continuum radiation in Earth’s magnetosphere (Kurth et al., 1981). Recent simulations suggest that UH waves generated near the reconnection X line may generate radio waves at the plasma frequency and second harmonic (Dokgo et al., 2019).

Langmuir and UH waves have been reported in magnetotail reconnection events. Farrell et al. (2002) reported UH waves in the separatrix regions close to the reconnection diffusion region. The UH waves were argued to be generated by electron beams, which were observed simultaneously with the waves (Farrell et al., 2003). Similarly, Viberg et al. (2013) reported Langmuir waves at the outer edge of the reconnection separatrix region where fast electron beams were observed. Evidence of Langmuir or beam-mode waves has been reported in kinetic simulations of reconnection in the separatrix regions (Fujimoto, 2014). Recent observations by the Magnetospheric Multiscale (MMS) spacecraft found UH waves in or near the electron diffusion regions of magnetotail reconnection (Burch et al., 2019; Li et al., 2021). These UH waves were shown to be generated by agyrotropic electron beams or crescent-shaped distributions, both at Earth’s magnetopause (Graham et al., 2017) and in the magnetotail (Burch et al., 2019).

Although there are several case studies Langmuir and UH waves in Earth’s magnetotail, statistical studies of these waves have been lacking. In this paper we perform a statistical study of plasma frequency waves in Earth’s magnetotail using the four Magnetospheric Multiscale (MMS) spacecraft. We show that while the occurrence rate of these waves is significantly lower than around Earth’s magnetopause, large-amplitude plasma frequency waves develop in the magnetotail. We investigate where these waves occur and how they are generated. We discuss how these waves are related to magnetic reconnection in Earth’s magnetotail. The outline of this paper is as follows: In section 2 we introduce the data used and present an overview of the plasma frequency waves observed by MMS. In section 3 we investigate the properties of the waves in the magnetotail and characterize the local plasma conditions where they are observed. In section 4 we investigate the electron distributions associated with the waves and discuss the sources of instability. In section 5 we describe

how the observed waves are related to magnetic reconnection in the magnetotail. Section 6 states the conclusions to this study.

2 Data and Overview

2.1 Data and Event Selections

To investigate the plasma frequency waves in Earth’s magnetotail we use the four MMS spacecraft, which orbit Earth in a tetrahedral configuration. In particular, we use the Electric field Double Probes (EDP) to measure the three-dimensional electric field. EDP consists of two instruments: the Spin-plane Double Probe (SDP) instrument (Lindqvist et al., 2016) and the Axial Double Probe (ADP) instrument (Ergun et al., 2016). To measure the electric field of plasma frequency waves we use the hfme data product, which nominally consists of snapshots sampling the electric field \mathbf{E} at 65.536 kHz over two second intervals. This sampling rate resolves the plasma frequency f_{pe} in the magnetotail and at the magnetopause, but is typically too slow to resolve the electron plasma frequency f_{pe} in Earth’s magnetosheath. These snapshots are only available during burst mode selections by the Scientist-In-The-Loop (SITL) (Fuselier et al., 2016) and have a nominal duty cycle of 25 % (Ergun et al., 2016). As a result, the intervals where burst mode data are available are typically regions considered interesting based on low-resolution data. For the magnetotail the selections are biased toward crossings of the plasma sheet boundary layer (PSBL), events with reconnection signatures, and jet fronts. The continuous burst mode \mathbf{E} is sampled at 8.192 kHz and very rarely resolves f_{pe} . We also use the FluxGate Magnetometer (FGM) to measure the background magnetic field \mathbf{B} (Russell et al., 2016), and the Fast Plasma Investigation (FPI) to measure the particle distributions and moments (Pollock et al., 2016). In burst mode the electron distributions and moments are sampled every 30 ms, while the ion distributions and moments are sampled every 150 ms. In fast survey mode the electron and ion distributions and moments are sampled every 4.5 s.

We note that on 2018 June 07 the electron spectrometers on MMS4 experienced a partial failure, so reliable electron moments and distributions cannot be obtained from this point onwards. For the snapshots captured over this time by MMS4 we use electron moments from MMS3 to calculate the plasma properties. Since the spacecraft typically remained in a close tetrahedral formation, this does not significantly affect the statistical results. However, when comparing the snapshots with electron distribution functions in section 4, we only use

MMS4 data when the electron spectrometers were fully operational. Finally, we note that on 2016 June 12 probe 4 of SDP on MMS4 became unbiased due to a dust impact on the SDP wire boom. However, the quality of the high-frequency electric field is unaffected. On 2018 September 21 probe 2 of SDP on MMS2 failed. Thus, after this time single ended measurements from probe 1 were required to produce the hmfe electric field. For the plasma frequency waves this does not significantly affect the waveform.

For this study we search through all hmfe snapshots from May 2017 to June 2022 for waves at the plasma frequency. We use the same search criteria as (Graham et al., 2018). To identify plasma frequency waves we bandpass filter \mathbf{E} above $f_{pe}/1.5$, where f_{pe} is calculated from the median n_e over the snapshot time. Snapshots with peak electric field above 5 mV m^{-1} are selected. Snapshots with broadband \mathbf{E} fluctuations, but no clear spectral peak near f_{pe} are excluded. Over this time we identify 110,079 hmfe snapshots with plasma frequency waves with maximum electric field E_{max} exceeding 5 mV m^{-1} . For each snapshot we calculate the median plasma properties over the snapshot interval from burst mode FGM and FPI data. The apogee of MMS over this time was $\sim 25 - 30 R_E$, where R_E is Earth's radius: The orbit of MMS processed so data is collected at the dayside, flanks, and magnetotail near the equatorial plane (Fuselier et al., 2016). Most of the snapshots with plasma frequency waves are found near Earth's magnetopause and in Earth's electron foreshock region, with a smaller fraction observed in Earth's magnetotail.

2.2 Langmuir and Upper Hybrid Wave Properties

To characterize the observed waves we calculate the fraction F_E of perpendicular power to total power of the snapshot:

$$F_E = \frac{\sum E_{\perp}^2}{\sum E_{\perp}^2 + \sum E_{\parallel}^2}, \quad (1)$$

where sums are over the whole hmfe snapshot, and E_{\parallel} and E_{\perp} are the magnitudes of \mathbf{E} parallel and perpendicular to \mathbf{B} . To calculate F_E we rotate \mathbf{E} into field aligned coordinates. We apply this calculation of F_E to all snapshots with plasma frequency waves.

As examples of the types of waves observed by MMS, Figure 1 shows two hmfe snapshots observed in Earth's magnetotail. Figures 1a–1c show a Langmuir wave, while Figures 1d–1f show an UH wave packet. The Langmuir wave is characterized by the electric field fluctuations along \mathbf{B} , as seen in Figure 1a. From the waveform we calculate $F_E = 0.08$. Figure 1b shows that the wave power peaks at about 1.8 kHz, just above the electron plasma

frequency f_{pe} estimated from the electron moments. In Figure 1c we plot F_E as a frequency-time spectrogram. For clarity, F_E is only shown for powers exceeding $10^{-6}P_{\max}$, where P_{\max} is the maximum power in the snapshot. We see that F_E is small at the frequencies where the power peaks, which accounts for the overall small value of F_E . We see that at slightly lower frequencies F_E tends to be close to 1.

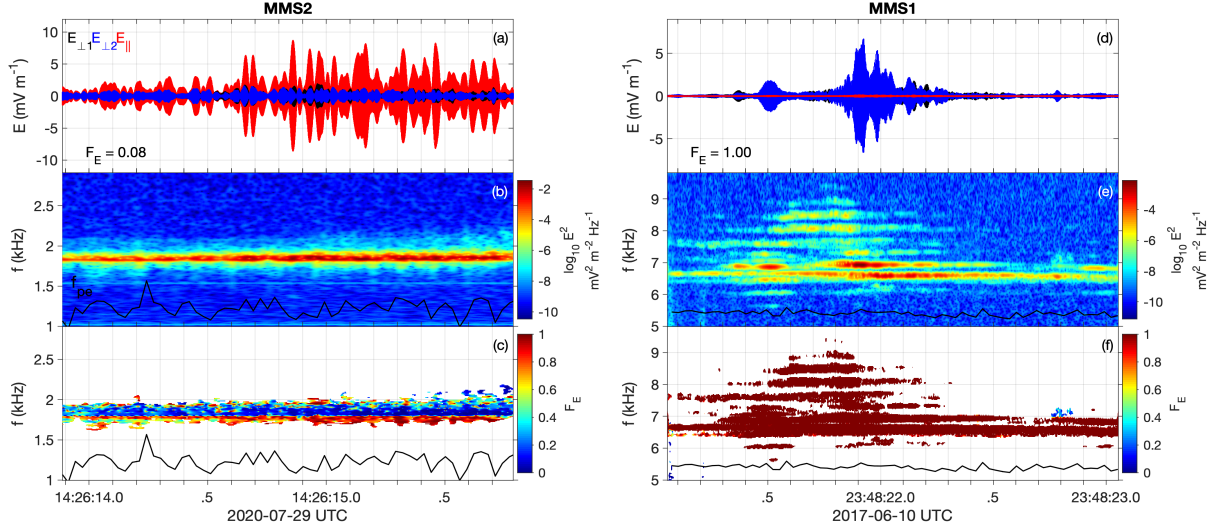


Figure 1. An example of a Langmuir wave and an UH wave observed in Earth’s magnetotail. Panels (a)–(c) show a Langmuir wave and panels (d)–(f) show an UH wave. (a) and (d) show the \mathbf{E} waveforms in field-aligned coordinates, (b) and (e) frequency-time spectrograms of \mathbf{E} power, (c) and (f) frequency-time spectrograms of F_E . The black lines show f_{pe} calculated from n_e .

The UH wave in Figure 1d is characterized by $E_{\perp} \gg E_{\parallel}$, resulting in $F_E \approx 1$. Figure 1e shows that the peak power occurs just below 7 kHz, which is just above f_{pe} calculated from the electron moments. The waves have frequencies in distinct bands separated by the electron cyclotron frequency f_{ce} , indicating that there are electron Bernstein waves in addition to the UH wave. Figure 1e shows that $F_E \approx 1$ for both the UH and Bernstein waves.

Both Langmuir and UH waves lie on the same dispersion surface. Figure 2a shows the dispersion surface for Langmuir and UH waves. The dispersion surface is calculated using WHAMP (waves in homogeneous, anisotropic, multicomponent plasmas) for a single isotropic Maxwellian distribution (Rönnmark, 1982). The plasma conditions used are electron number density $n_e = 0.1 \text{ cm}^{-3}$, electron temperature $T_e = 500 \text{ eV}$, and magnetic field

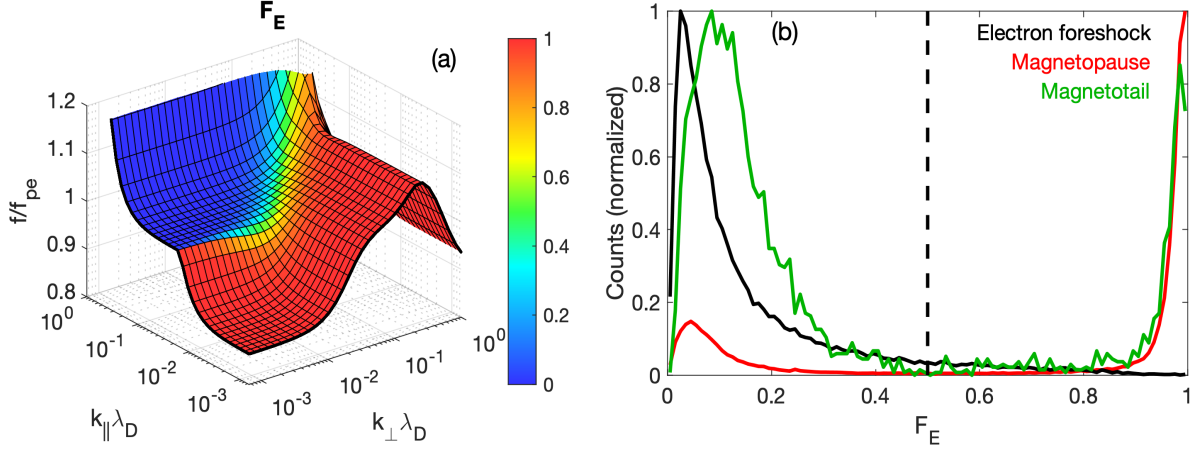


Figure 2. Dispersion surface of Langmuir/UH waves and statistics of F_E . (a) Theoretical dispersion surface of Langmuir/UH waves. The dispersion surfaces shows the frequency versus k_{\parallel} , k_{\perp} , and frequency f . The wave numbers are normalized with the electron Debye length λ_D and the frequency is normalized by the electron plasma frequency f_{pe} . The color indicates the value of F_E as a function of k_{\parallel} and k_{\perp} . (b) The distribution of F_E observed by MMS in the electron foreshock (black), near the magnetopause (red), and in the magnetotail (green). The black dashed line indicates $F_E = 0.5$.

magnitude $|\mathbf{B}| = 30$ nT, corresponding to typical magnetotail conditions. The color shading indicates F_E as a function of frequency f and wave numbers parallel and perpendicular to \mathbf{B} , k_{\parallel} and k_{\perp} , respectively. For Langmuir waves with $k_{\parallel} \gg k_{\perp}$, F_E is close to 0. At low k_{\parallel} the Langmuir wave couples to the electromagnetic Z-mode, where $F_E \approx 1$. For UH waves with $k_{\perp} \gg k_{\parallel}$, $F_E \approx 1$. We find that intermediate values of F_E only occur when k_{\parallel} and k_{\perp} are comparable, corresponding to oblique Langmuir waves. However, in observations intermediate values of F_E can result from Langmuir and UH waves being observed in the same snapshot. We will use the value of F_E to distinguish between Langmuir and UH waves in the following sections.

2.3 Statistical Results

We now proceed to studying plasma frequency waves statistically. In Figure 2b we plot the histograms of F_E for all plasma frequency waves in our dataset. We divide the waves into three groups based on where they are observed: In the electron foreshock, near the magnetopause, and in the magnetotail. The electron foreshock waves are all plasma

frequency waves observed when MMS was in the solar wind. The solar wind times are taken from the SDP region calibration files, which flag the times MMS was in the solar wind, magnetosheath, and magnetospheric regions. The vast majority of plasma waves where observed in the electron foreshock, where the magnetic field was connected to the bowshock, rather than the pristine solar wind, where large-amplitude plasma frequency waves are extremely rare. We consider magnetotail waves to be those found inside a cylinder defined by $X_{GSM} < -5 R_E$ and $\sqrt{Y_{GSM}^2 + Z_{GSM}^2} < 10 R_E$. The remaining snapshots we consider to be close to the magnetopause. Due to the nominal Nyquist frequency of the hmfe data, plasma waves in the magnetosheath are typically not resolved (Graham et al., 2018). Using these criteria we find 43664 snapshots in the electron foreshock, 63535 snapshots near the magnetopause, and 2880 snapshots in the magnetotail.

Figure 2b shows that the statistical distribution of F_E varies depending on the plasma region. At the magnetopause and in the magnetotail the waves are characterized by either F_E close to 0 and close to 1. We find that very few waves are characterized by intermediate values of F_E . A higher proportion of low- F_E waves are observed in the magnetotail than for near the magnetopause. In the electron foreshock most waves are characterized by F_E close to zero and the number of snapshots as a function of F_E decreases as F_E increases. In contrast to the magnetopause and magnetotail, there is no peak in F_E near 1. Thus the statistical properties of the waves depend on the plasma region.

To determine the type of plasma frequency waves we observe in a given snapshot we define Langmuir waves as snapshots with $F_E < 0.5$ and UH waves as snapshots with $F_E > 0.5$. Using these definitions we find that near the magnetopause 31 % of the waveforms are Langmuir waves, while the remaining waves are UH waves. Thus, UH waves are significantly more common than Langmuir waves near the magnetopause. This is consistent with previous observation by (Graham et al., 2018), where 35 % of the waveforms were classified as Langmuir waves. In contrast, when using the same definition for the magnetotail region we find that 78 % of the snapshots are Langmuir waves, meaning that Langmuir are substantially more common than UH waves. This might suggest that statistically there are different processes generated the waves, compare with near the magnetopause. Finally, in the electron foreshock 93 % of the waves are identified as Langmuir waves. Since, we do not observe waveforms with $F_E \approx 1$, purely UH waves do not occur in the electron foreshock.

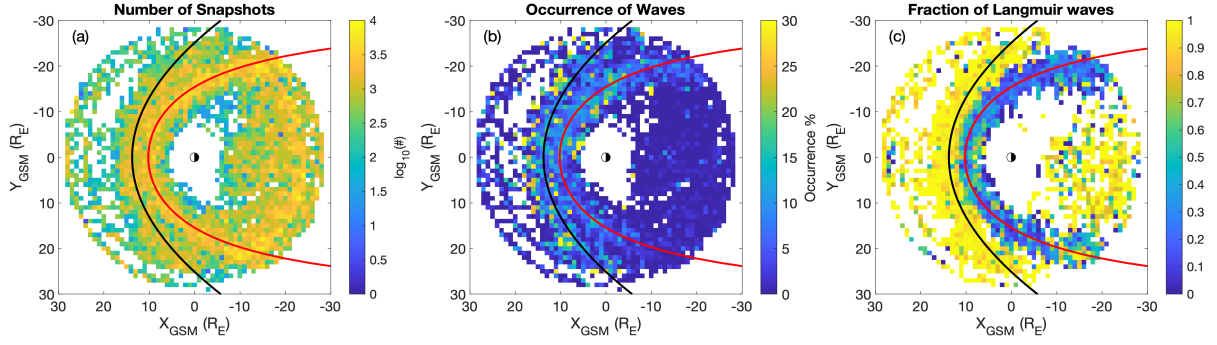


Figure 3. Statistical occurrence of Langmuir and UH waves versus position as observed by MMS. (a) Number of hmfe snapshots where plasma frequency waves are potentially observable versus X and Y position in GSM coordinates. (b) Percentage of snapshots where plasma frequency waves are observed with $E_{\max} > 5 \text{ mV m}^{-1}$ versus position. (c) Fraction of Langmuir waves with $F_E < 0.5$ to all plasma frequency waves versus position. The red and black lines indicate the average locations of the magnetopause and bowshock.

We now investigate the occurrence of plasma frequency waves as a function of position. To calculate the occurrence percentage we divide the number of hmfe snapshots with plasma frequency waves to the total number of hmfe snapshots where plasma frequency waves could potentially be observed in a given region. We consider plasma frequency waves to be potentially observable if the median electron plasma frequency f_{pe} estimated from FPI electron moments across the hmfe snapshot is below the Nyquist frequency of the snapshot. To calculate these occurrence percentages we calculate two-dimension histograms in the Geocentric Solar Magnetic (GSM) X and Y directions. The width of the bins is $1 R_E$. The results are shown in Figure 3. Figure 3a shows the total number of snapshots as a function of X and Y in GSM coordinates. A large number of snapshots are observed at the bowshock, magnetopause, and throughout the magnetotail. At the magnetopause the counts remain high all along the magnetopause from the subsolar point to past the terminator $X < 0$ along both flanks.

In Figure 3b we plot the occurrence percentage of plasma frequency waves from hmfe snapshots as a function of position. Figure 3b shows that the probabilities tend to be highest along the magnetopause, extending from the subsolar point to the far flanks. We find that the occurrence rate tends to be higher on the dawn side ($Y < 0$) compared with the dusk flank ($Y > 0$). The occurrence in the magnetotail is substantially smaller than near the

magnetopause. Near the bowshock and in the solar wind the occurrence is highly variable. Whether waves are observed primarily depends on the spacecraft position in relation to the electron foreshock, which depends on the solar wind \mathbf{B} direction.

In Figure 3c we plot the fraction of hmfe snapshots classified as Langmuir waves to the total number of snapshots with plasma frequency waves as a function of position. We see that near the foreshock and throughout the magnetotail Langmuir waves are more common than UH waves. In contrast, all along the magnetopause UH waves are significantly more common than Langmuir waves.

3 Magnetotail Plasma Waves

In this section we now focus exclusively on the waves in the magnetotail. We investigate the properties of the Langmuir and UH waves, and where the waves occur by comparing with the local plasma conditions. In Figure 4a we plot the histograms of the maximum electric field magnitude E_{\max} associated with each snapshot for Langmuir and UH waves. As expected the highest counts are at the lowest E_{\max} close to the threshold. For Langmuir waves the counts are significantly higher than for UH waves for all E_{\max} , except for the very highest E_{\max} . Thus, we do not see any clear dependence on the relative proportion of Langmuir and UH waves with E_{\max} . As a result, the threshold condition $E_{\max} > 5 \text{ mV m}^{-1}$ should not significantly affect the relative proportion of Langmuir and UH waves observed in the magnetotail.

In Figure 4b we plot histograms of f_{pk}/f_{pe} for Langmuir waves and f_{pk}/f_{uh} for UH waves, where f_{pk} is the frequency at which the wave power peaks, $f_{uh} = \sqrt{f_{pe}^2 + f_{ce}^2}$ is the upper hybrid frequency, and f_{ce} is the electron cyclotron frequency. To calculate f_{pe} and f_{uh} we use the median values n_e and \mathbf{B} over the snapshot times. In the magnetotail n_e can be extremely low so counting statistics in the electron spectrometers will also be low, resulting in some uncertainty in the moments. To minimize the effects of internal photoelectrons (Gershman et al., 2017), we calculate the moments from the partial moments product for electron energies above 50 eV in the magnetotail. Thus, the histograms of f_{pk}/f_{pe} and f_{pk}/f_{uh} for Langmuir and UH waves can provide an indicator of the reliability of n_e estimated from particle data. Figure 4b shows that the histograms of f_{pk}/f_{pe} and f_{pk}/f_{uh} peak around 1, as expected for Langmuir and UH waves. For Langmuir waves the median f_{pk}/f_{pe} is 1.1 with standard deviation of 0.4, while for UH waves the median

f_{pk}/f_{uh} is 1.0 with a standard deviation of 0.3. Therefore, Langmuir and UH are generally found close to f_{pe} and f_{uh} , as expected. Statistically, the values of f_{pk}/f_{pe} and f_{pk}/f_{uh} for Langmuir and UH waves tend to increase as n_e decreases for $n_e \lesssim 0.01 \text{ cm}^{-3}$. Cases where there are significant deviations from 1 likely result from the uncertainty in n_e .

In Figure 4c we plot the histograms of electron temperature T_e for Langmuir and UH waves. For Langmuir waves we calculate a median T_e of 480 eV and a standard deviation of 600 eV, while for UH waves the median T_e is 600 eV and a standard deviation of 1.4 keV. Thus, we tend to observe UH waves over a broader range of T_e than Langmuir waves. In particular, we are more likely to observe Langmuir waves than UH waves for $T_e \lesssim 3 \text{ keV}$, while for $T_e \gtrsim 3 \text{ keV}$ UH waves become more likely to be observed than Langmuir waves. Figure 4d shows that the majority of the waves are observed for $1 \lesssim f_{pe}/f_{ce} \lesssim 10$. Thus, the waves are primarily observed for weakly magnetized plasma conditions, with only a small fraction of the waves occurring for $f_{pe}/f_{ce} < 1$. We note that for $f_{pe}/f_{ce} \gtrsim 10$ the number of counts of Langmuir and UH waves becomes more comparable.

In Figure 5 we investigate the statistical plasma properties, to determine where the waves are observed in relation to the magnetotail plasma sheet. We calculate the histograms of Langmuir and UH waves versus B_x in GSM coordinates and the ion plasma beta β_i (Figures 5a–5b). Figure 5a shows that most Langmuir waves are observed for $B_x > 0$, with the counts peaking for $B_x \sim 20 \text{ nT}$. A smaller peak is seen at $B_x \sim -20 \text{ nT}$ for Langmuir waves, indicating that most of the waves are observed northward of the magnetotail plasma sheet. This is because MMS spends more time above the plasma sheet, which is due to the spacecraft orbit. For both Langmuir and UH waves very few snapshots are observed for $B_x \sim 0$, suggesting that very few waves are observed near the center of the plasma sheet where B_x is small.

Figure 5b shows that the counts of Langmuir and UH waves versus β_i . The blue and green dashed lines indicate $\beta_i = 0.01$ and $\beta_i = 0.5$, which correspond to the typical transition from the lobes to the plasma sheet boundary layer (PSBL), and plasma sheet to central plasma sheet (Haaland et al., 2010). We find that the Langmuir wave counts peaks around $\beta_i = 0.02$, which corresponds to β_i typical of the PSBL. For $\beta_i > 0.02$ the counts decrease as β_i increases for Langmuir waves, and only a small number of counts are observed for $\beta_i > 0.5$, meaning very few Langmuir waves are seen in or near the central plasma sheet. Only a small fraction of the Langmuir waves are observed for $\beta_i < 0.01$, which corresponds

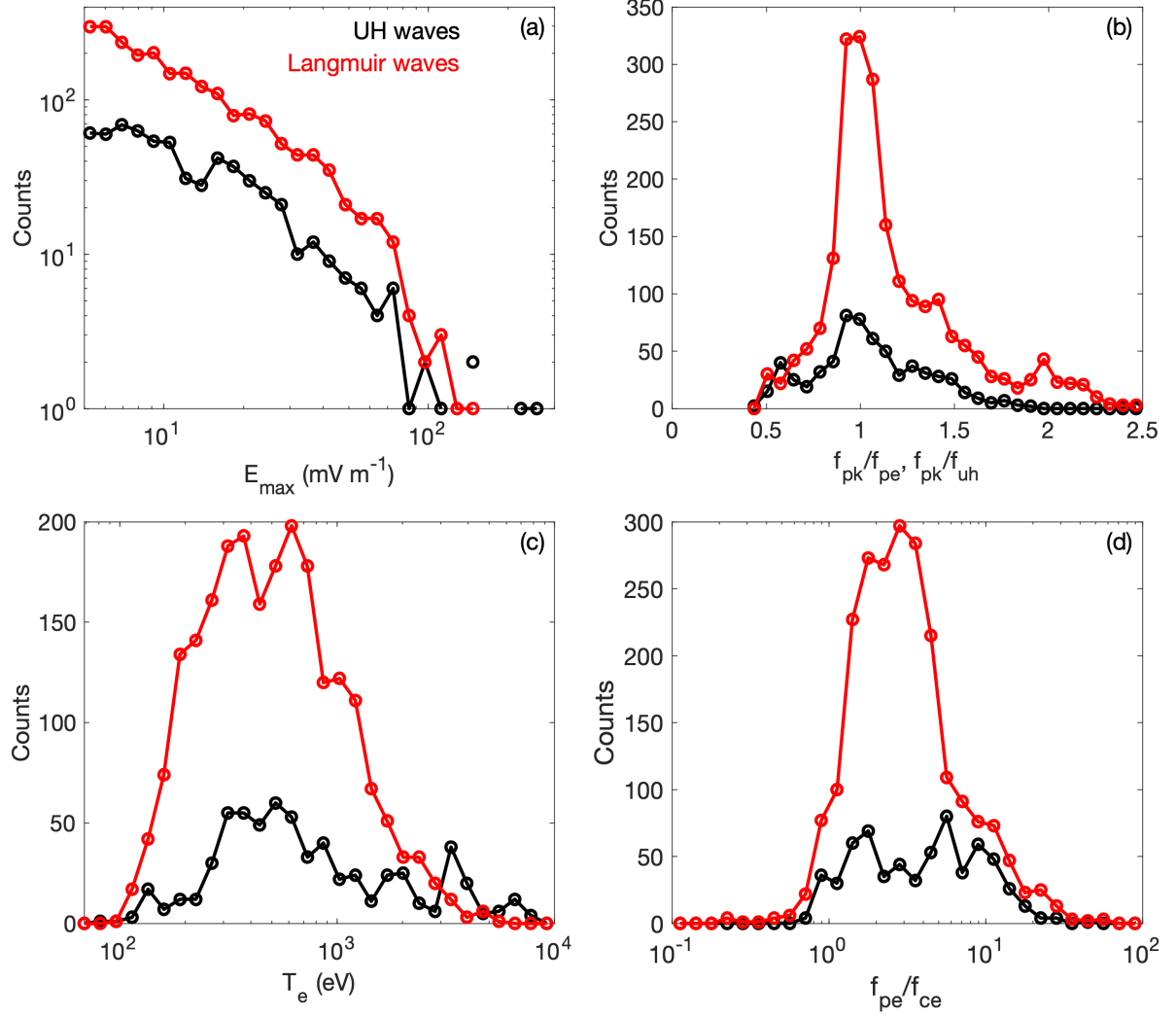


Figure 4. Statistical plots of the properties of Langmuir and UH waves in Earth's magnetotail.

(a) Histograms of maximum electric field E_{\max} for Langmuir waves (red) and UH waves (black). (b) Histograms of f_{pk}/f_{pe} for Langmuir waves (red) and f_{pk}/f_{uh} (black), where f_{pk} is the frequency at which the wave power peaks. (c) and (d) Histograms of T_e and f_{pe}/f_{ce} associated with Langmuir and UH waves.

to the lobe plasma. For UH waves we find that there are two peaks in the counts. The first peak is at $\beta \sim 0.02$, corresponding to the PSBL, and the second peak is at $\beta_i \approx 1$, corresponding to near the central plasma sheet.

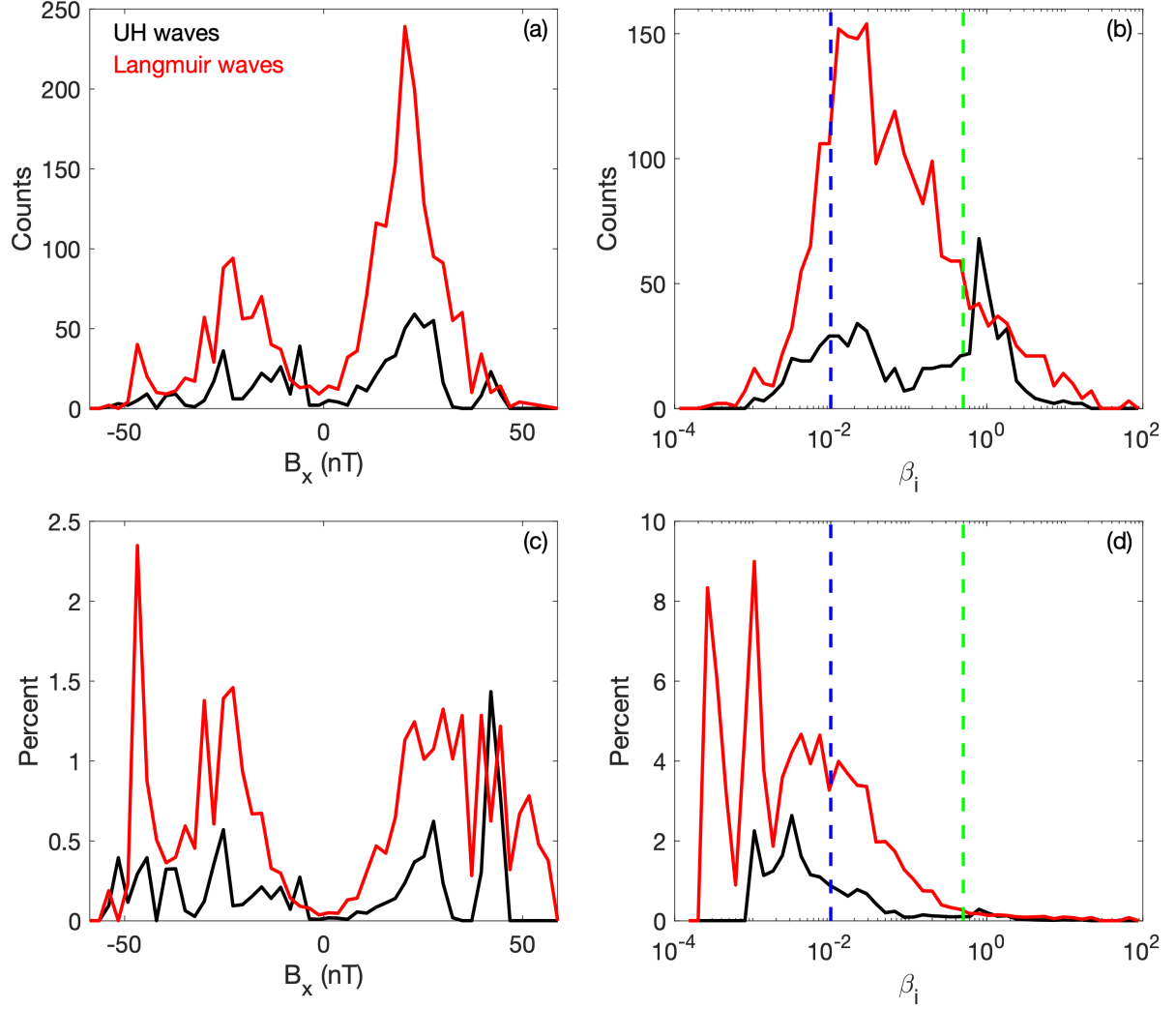


Figure 5. Statistical plots of Langmuir and UH waves in Earth's magnetotail. Histograms of Langmuir (red) and UH waves (black) versus (a) B_x in GSM coordinates and (b) β_i . Occurrence rates as percentages of Langmuir (red) and UH waves (black) versus (c) B_x . and (d) β_i . The blue and green dashed lines in panels (b) and (d) are $\beta_i = 0.01$ and $\beta_i = 0.5$, which approximately indicate the PSBL and boundary of the central plasma sheet, respectively.

We now investigate the occurrence rates as percentages by dividing the number of snapshots with Langmuir or UH waves by the total number of snapshots where plasma

frequency waves could potentially be observed. We only consider snapshots captured in the magnetotail region as defined in section 2.3. We calculate these occurrence rates as functions of B_x , and β_i (Figures 5c–5d). Figure 4c shows the occurrence percentage of Langmuir and UH waves versus B_x . We find that the probability of finding Langmuir and UH waves above and below the plasma sheet are comparable, despite the counts being higher for above the plasma sheet where $B_x > 0$. For Langmuir waves the occurrence percentage is $\approx 1\%$ for $15 \text{ nT} \lesssim |B_x| \lesssim 40 \text{ nT}$, which is consistent with the lobe or PSBL regions. For UH waves the percentage is below 0.5% due to UH waves being much less common in the magnetotail. For both UH and Langmuir waves the probabilities are very low near the central plasma sheet for $B_x \approx 0$.

In Figure 5d we find that the occurrence percentage for Langmuir waves peaks at $\approx 4\%$ just below $\beta_i = 0.01$, suggesting that Langmuir waves are most likely to be observed at or near the PSBL for lobe-like plasma conditions. As β_i increases the percentage decreases meaning the probability of observing Langmuir waves decreases as the center of the current sheet is approached. A similar result is observed for UH waves, except the peak probability occurs for $\beta_i \sim 3 \times 10^{-3}$. Despite there being a clear peak in the counts at $\beta_i \approx 1$, the probability at this β_i is extremely small. We note that the statistics become very unreliable for $\beta_i \lesssim 10^{-3}$, both due to the low number of snapshots with and without waves and the increased uncertainty in the particle moments required to compute β_i . Thus, peaks in probability of Langmuir waves for $\beta_i \lesssim 10^{-3}$ are questionable.

In summary, we primarily observe Langmuir waves in or near the PSBL and a relatively small number of Langmuir waves in the central plasma sheet. We find that UH waves are observed both in the PSBL and near the central plasma sheet. However, when we consider the occurrence rates of Langmuir and UH waves in the magnetotail, we find that occurrences are highest in the PSBL or in the lobe. The occurrence is extremely small in the central plasma sheet.

4 Source of waves

In this section we investigate the sources of instability for Langmuir and UH waves in Earth’s magnetotail by comparing the local electron distributions with the associated waves. We start by considering case studies to show the types of electron distributions associated with the waves, then proceed to a statistical investigation.

4.1 Case studies

We first consider the source of Langmuir waves in Earth's magnetotail. Langmuir waves are well known to be generated by electron beams via the bump-on-tail instability, so evidence of electron beams is expected. We frequently see evidence of electron beams in association with Langmuir waves in the magnetotail. Figure 6 shows an example of Langmuir waves and the associated electron distributions observed by MMS1 on 2017 July 09. Figure 6a shows the waveform of \mathbf{E} , which is characterized by $E_{\parallel} \gg E_{\perp}$, corresponding to $F_E = 0.11$. For this event the average background conditions are $n_e \approx 0.06 \text{ cm}^{-3}$, $T_e \approx 260 \text{ eV}$, and $|\mathbf{B}| = 29 \text{ nT}$, which are consistent with lobe plasma conditions. The wave is observed at $f_{pe} \approx 2.5 \text{ kHz}$ (Figure 6b). In Figure 6c we plot the one-dimensional reduced electron distributions along \mathbf{B} as a function of time. The distributions are characterized by a core lobe electron population, and a significant enhancement in the electron phase-space density f_e at superthermal electron speeds antiparallel to \mathbf{B} . We find that this enhancement remains throughout the duration of the snapshot.

For this event n_e is very low, resulting in low counting statistics in the particle distributions. Therefore, to obtain clear distribution functions we average over all the distributions observed over the time of the snapshot (2 seconds or 66 distributions). The resulting distributions are shown in Figures 6d–6f. Figure 6d shows the two-dimensional reduced distribution in the v_{\parallel} – $v_{\perp 1}$ plane, where v_{\parallel} is the electron speed aligned with \mathbf{B} and $v_{\perp 1}$ is the electron speed in the direction of the median electron bulk velocity perpendicular to \mathbf{B} . To avoid photoelectrons and internal photoelectrons (Gershman et al., 2017) in the reduced distributions we neglect electron energy channels below 50 eV when computing the distributions. We see an approximately isotropic core population, corresponding to the lobe plasma, and an electron beam antiparallel to \mathbf{B} with speed centered around $v_{\parallel} = 4 \times 10^4 \text{ km s}^{-1}$. For this event the electron thermal speed is $v_e = \sqrt{2k_B T_e / m_e} = 9.6 \times 10^3 \text{ km s}^{-1}$. The corresponding ratio of beam speed to electron thermal speed is $v_b / v_e \approx 4.4$. We estimate the beam density to be $n_b \approx 6 \times 10^{-3} \text{ cm}^{-3}$, corresponding to $n_b / n_e \approx 0.01$. These beam properties are consistent with the properties required to generate Langmuir waves. Figures 6e and 6f show the pitch-angle distributions versus electron energy E_e for pitch angles 0° , 90° , and 180° , and pitch angle θ for constant electron energies. We see clear enhancements in f_e at $\theta = 180^\circ$ for $1 \text{ keV} \lesssim E \lesssim 30 \text{ keV}$. Figure 6e shows that there is little positive slope in f_e associated with the beam. Thus, the distribution is likely close to marginal stability. Strong positive slopes are unlikely to be directly observed in association with large-amplitude Lang-

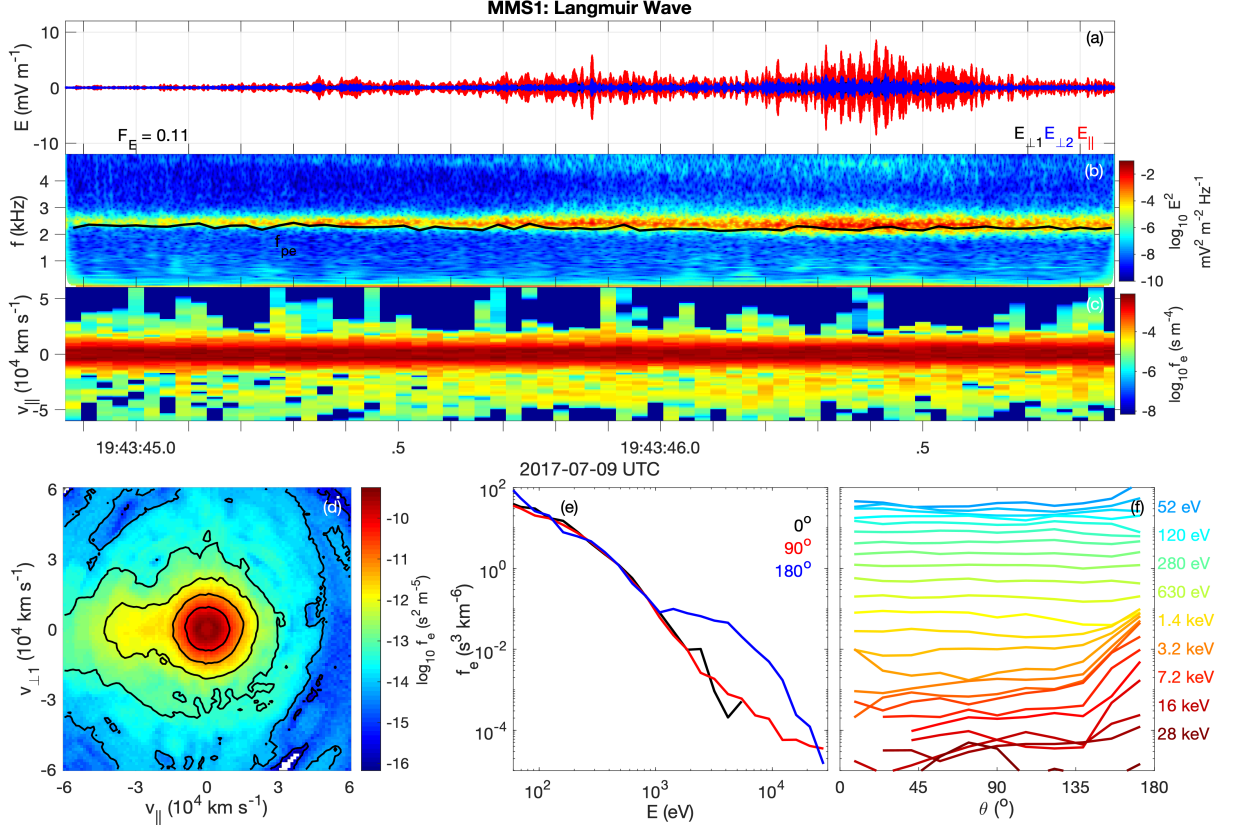


Figure 6. Snapshot of Langmuir waves and the associated electron distributions observed by MMS1 on 2017 July 09. (a) Electric field waveform in field-aligned coordinates. (b) Electric field spectrogram. The black line is f_{pe} calculate from the electron moments. (c) One-dimensional reduced electron distribution parallel to \mathbf{B} . (d) Two-dimensional reduced electron distribution in the plane of \mathbf{B} and the perpendicular electron bulk velocity. (e) Electron phase-space density f_e versus E_e for pitch angles $\theta = 0^\circ$ (black), 90° (red), and 180° (blue). (f) f_e versus θ for constant energies (blue corresponds to low E_e while red corresponds to high E_e). The distributions in (d)–(f) are average distributions over the snapshot time.

muir waves because such distributions would be rapidly stabilized, leading to plateau-like
 enhancements, as seen in Figures 6d and 6e. Figure 6f shows that the beam is very narrow
 in pitch angle θ , meaning the beam electrons remain closely aligned with \mathbf{B} . We conclude
 that the observed waves are generated by the bump-on-tail/beam-plasma instability.

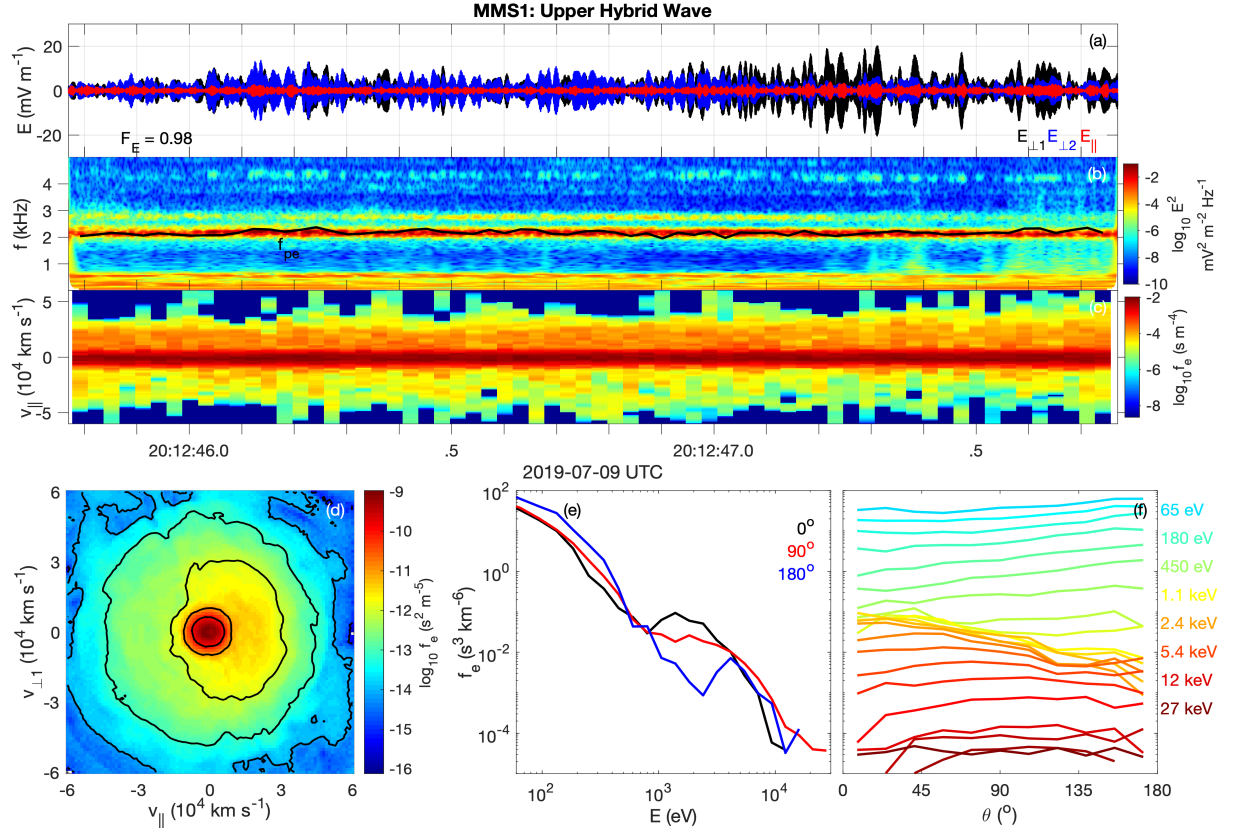


Figure 7. Snapshot of UH waves and the associated electron distributions observed by MMS1 on 2019 July 09. (a) Electric field waveform in field-aligned coordinates. (b) Electric field spectrogram. The black line is f_{pe} calculate from the electron moments. (c) One-dimensional reduced electron distribution parallel to \mathbf{B} . (d) Two-dimensional reduced electron distribution in the plane of \mathbf{B} and the perpendicular electron bulk velocity. (e) f_e versus electron energy for $\theta = 0^\circ$ (black), 90° (red), and 180° (blue). (f) f_e versus θ for constant E_e (blue corresponds to low E_e while red corresponds to high E_e). The distributions in (d)–(f) are averaged distributions over the snapshot time.

The second case study, shown in Figure 7, is an UH wave and the associated electron distributions observed by MMS1 on 2019 July 09. The local plasma conditions are $|\mathbf{B}| = 43$ nT, $n_e = 0.06$ cm⁻³, and $T_e = 340$ eV. The panels in Figure 7 are in the same format as Figure 6. For this snapshot $E_\perp \gg E_\parallel$ and $F_E = 0.98$, so the waveform is identified as an

UH wave (Figure 7a). The wave has a peak frequency at $f_{pe} \approx 2$ kHz, as shown in Figure 7b. From the one-dimensional reduced electron distributions parallel to \mathbf{B} we see that there is a cold lobe core population and a beam-like population drifting parallel to \mathbf{B} (Figure 7c). In the averaged two-dimensional reduced distribution, shown in Figure 7d, we observe an approximately isotropic core population and a superthermal beam-like component for $v_{\parallel} \gtrsim 0$. This beam is very broad in the directions perpendicular to \mathbf{B} , in contrast to the narrow beam in Figure 6. This is seen in Figure 9f, where for superthermal energies f_e decreases as θ increases over all θ . For this distribution we estimate beam density to be $n_b/n_e \sim 0.1$, which is significantly higher than n_b/n_e in Figure 6. This distribution may be interpreted as a loss-cone distribution because f_e is significantly reduced at θ close to 180° . This is seen in Figure 7e, which shows that f_e at $\theta = 180^\circ$ is substantially smaller than f_e at $\theta = 90^\circ$ for $1 \text{ keV} \lesssim E_e \lesssim 4 \text{ keV}$. The likely source of instability is either the broad electron beam or loss-cone distribution at superthermal energies.

Figure 7 represents the most common type of potentially unstable electron distribution associated with UH waves in the magnetotail. However, we note two other types of potentially unstable electron distributions where UH waves are observed: (1) We observe some UH waves in or near electron diffusion regions of magnetic reconnection, where agyrotropic electron distributions occur. (2) Some UH waves are observed closer to Earth where \mathbf{B} is approximately northward, corresponding more to the inner magnetosphere than Earth's magnetotail. These UH waves are associated with butterfly distributions, which are characterized by enhancements in f_e around pitch angles $\theta = 45^\circ$ and 135° . These waves tend to be associated with a series of electron Bernstein waves.

Figure 8 shows an example of UH waves observed near an electron diffusion region. An overview of the reconnection is shown in Figures 8a–8d. Figure 8a shows that \mathbf{B} reverses direction at 23:01:07 UT. Around this region we observe large electron bulk velocities parallel $V_{e,\parallel}$ and perpendicular $V_{e,\perp}$ to \mathbf{B} (Figure 8b). In Figures 8c and 8d we show the burst mode \mathbf{E} and the associated spectrogram. The UH waves are observed before the current sheet crossing, where $V_{e,\perp}$ starts to become large. Closer the center of the current sheet we observe large-amplitude \mathbf{E} fluctuations below f_{ce} . Figures 8e and 8f shows the hmfe snapshot of \mathbf{E} and the associated spectrogram. The snapshot was captured over the time indicated by the yellow-shaded region in Figures 8a–8c. These UH waves have peak amplitude of $\approx 270 \text{ mV m}^{-1}$ and are the largest amplitude waves we observe in the magnetotail in our dataset. The waves are characterized by $E_{\perp} \gg E_{\parallel}$ with $F_E = 0.94$.

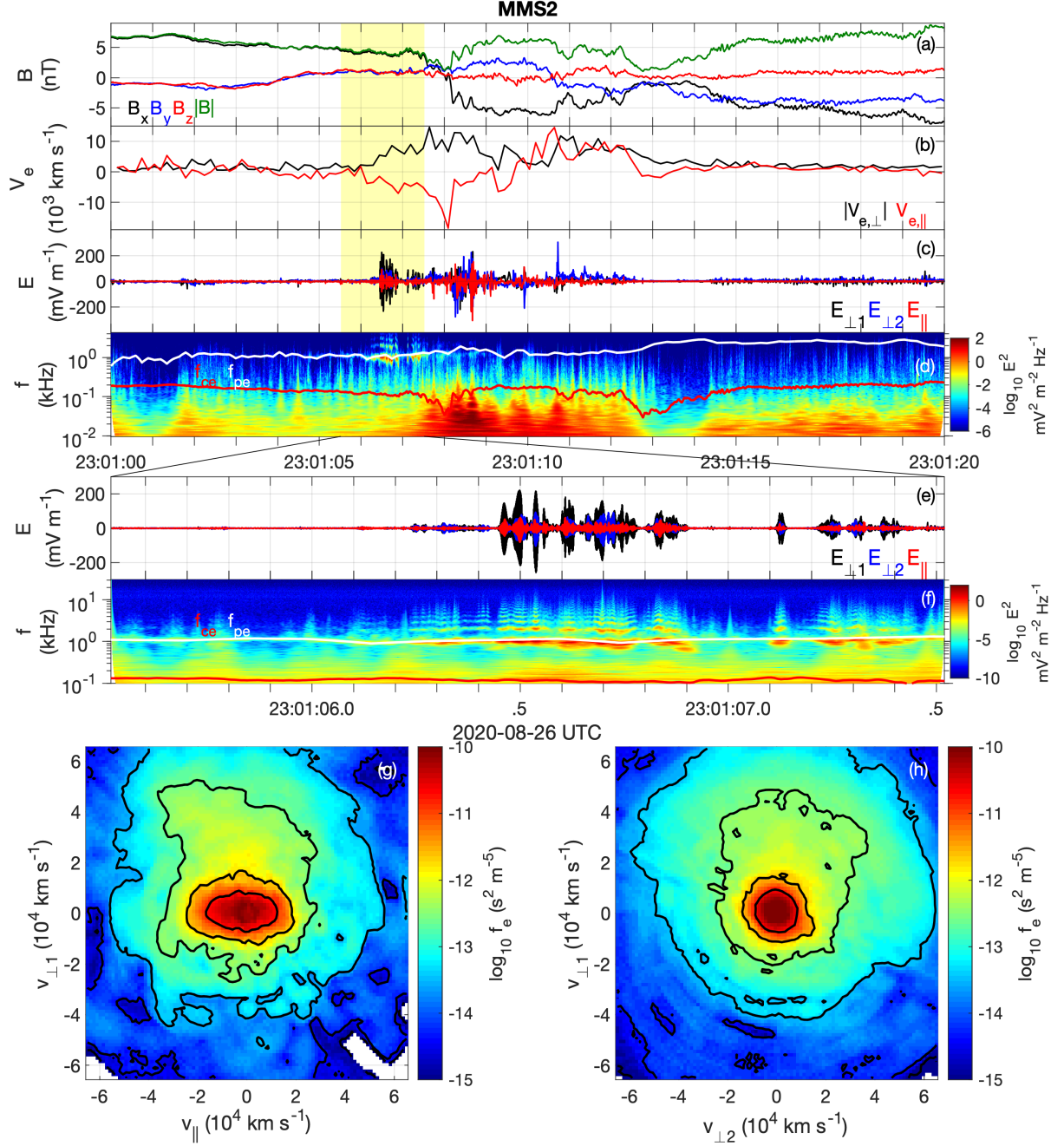


Figure 8. UH waves and agyrotropic electron distributions near an electron diffusion region observed by MMS2 on 2020 August 26. (a) \mathbf{B} in GSM coordinates. (b) Magnitude of electron velocity perpendicular to \mathbf{B} , $V_{e,\perp}$ (black) and parallel electron velocity $V_{e,\parallel}$ (red). (c) Burst mode \mathbf{E} in field-aligned coordinates. (d) Frequency-time spectrogram of burst mode \mathbf{E} . (e) and (f) hmfe electric field of UH waves in field-aligned coordinates and the associated frequency-time spectrogram. (g) and (h) Two-dimensional reduced electron distributions in the $v_{\parallel} - v_{\perp 1}$ and $v_{\perp 2} - v_{\perp 1}$ planes, where v_{\parallel} is aligned with \mathbf{B} , $v_{\perp 1}$ is aligned with $\mathbf{V}_{e,\perp}$, and $v_{\perp 2}$ is in the direction orthogonal to \mathbf{B} and $\mathbf{V}_{e,\perp}$.

In Figures 8g and 8h we plot the averaged two-dimensional reduced electron distributions over the time of the snapshot. Figure 8g shows that the electron distribution is characterized by a core electron population with a strong parallel temperature anisotropy, which is typical of magnetic reconnection inflow regions close to the X line (Egedal et al., 2008). Figure 8h shows that this core population is approximately gyrotropic. In addition, we also observe agyrotropic beam-like electrons in the direction of $\mathbf{V}_{e,\perp}$, which accounts for the large $V_{e,\perp}$ at the time the UH waves are observed. For the beam-like component we estimate $n_b/n_e \approx 0.016$. This beam density is consistent with previous observations of UH waves in or near electron diffusion regions (Graham et al., 2017; Burch et al., 2019).

By visual inspection of the electron distributions associated with UH waves we find that $\sim 2\%$ of the UH snapshots are observed in or near the electron diffusion region based on the associated electron distributions exhibiting agyrotropic features, such as in Figures 8g and 8h. Thus, the vast majority of UH waves are observed outside of the electron diffusion region, where the electron distributions are approximately gyrotropic. This is not surprising because encounters with the EDR are rare and only represent a small fraction of the available burst mode data.

In Figure 9 we show an example of UH waves and electron Bernstein waves observed in the inner magnetosphere by MMS1 on 2018 October 01. The spacecraft was located at $(-6.3, 2.1, -0.6) R_E$ in GSM coordinates. Figures 9a and 9b show the waveform of \mathbf{E} and the power spectrum of the perpendicular and parallel components of \mathbf{E} . From the power spectrum we see clear peaks just above the harmonics of f_{ce} , which are the electron Bernstein waves. The waves occur both above and below the upper hybrid frequency f_{uh} . In this case there is no clear difference between the spectral peaks associated with the Bernstein waves and the UH wave. Figures 9c and 9d show the electron distribution averaged of the snapshot interval. Figure 9c shows that the thermal part of the electron distribution is characterized by a square-like shape in the $v_{\parallel}-v_{\perp,1}$ plane. At higher speeds the distribution is approximately isotropic. At very low speeds there is a slight parallel temperature anisotropy. In Figure 9d we plot f_e versus θ for constant E_e . For $0.8 \text{ keV} \lesssim E_e \lesssim 5 \text{ keV}$, f_e has two peaks around $\theta = 45^\circ$ and 135° . These types of distributions are referred to as butterfly distributions. At higher E_e , f_e is approximately isotropic, while for low E_e , f_e peaks at $\theta = 0^\circ$ and 180° , correspond to a parallel temperature anisotropy. The butterfly distributions could be responsible for the observed UH and Bernstein waves because there are no other features in the distribution suggestive of instability. It is also possible that

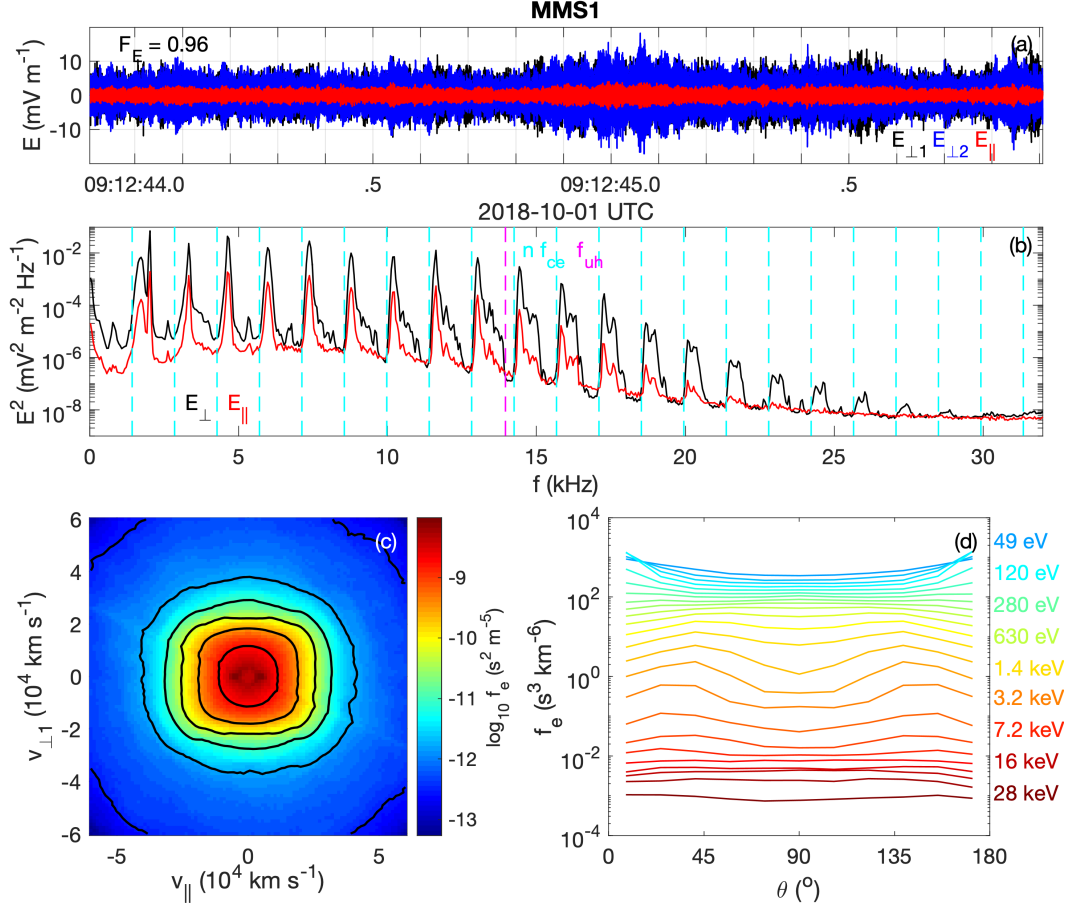


Figure 9. Example of UH and electron Bernstein waves in the inner magnetosphere observed by MMS1 on 2018 October 01. (a) Electric field waveform in field-aligned coordinates. (b) Power spectrum of the perpendicular (black) and parallel (red) electric fields. The cyan dashed lines show the f_{ce} and its harmonics and the magenta dashed shows f_{uh} . (c) Two-dimensional reduced electron distribution in the v_{\parallel} - $v_{\perp,1}$ plane. (d) f_e versus θ for constant E_e (blue corresponds to low E_e while red corresponds to high E_e). The distributions in (c)–(d) are averaged distributions over the snapshot time.

the butterfly distributions result from wave-particle interactions with the waves. Of the UH wave snapshots in the magnetotail about 14 % are classified as being in the inner magnetosphere where \mathbf{B} is approximately northward, with similar features to those in Figure 9.

4.2 Statistical results

We now consider the electron distributions associated with Langmuir and UH waves statistically. For each snapshot with Langmuir and UH we average the electron distribution over the snapshot duration. To find evidence of electron beams or the remnants of electron beams we plot f_{\parallel}/f_{\perp} , where f_{\parallel} is the electron phase-space density from the pitch-angle distribution either parallel or anti-parallel to \mathbf{B} . For each of the electron pitch-angle distribution we plot f_{\parallel}/f_{\perp} in the beam direction and anti-aligned with the beam direction. We define the beam direction to be the direction with largest $\sum f_{\parallel}/f_{\perp}$ for $E_e > 500$ eV.

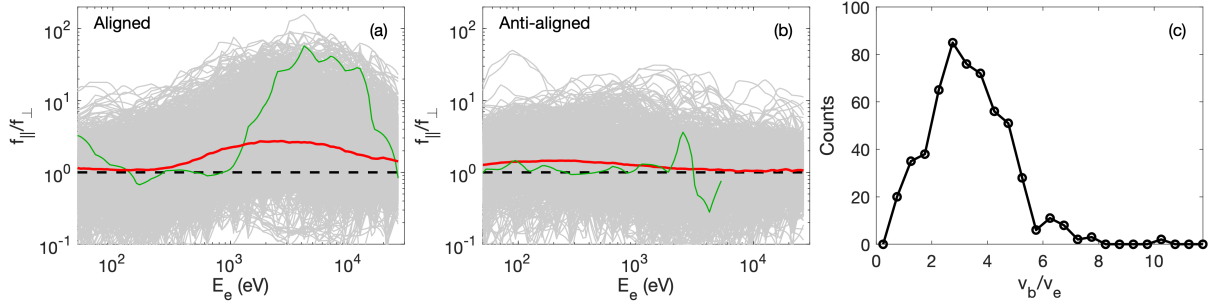


Figure 10. Statistical properties of the electron distributions associated with Langmuir waves. (a) Plot of f_{\parallel}/f_{\perp} versus E_e in the electron beam direction for all electron distributions associated with Langmuir waves (gray lines). (b) Plot of f_{\parallel}/f_{\perp} versus E_e for the direction anti-aligned with the beam for all electron distributions associated with Langmuir waves. The red curves are the median f_{\parallel}/f_{\perp} of all distributions as a function of E_e and the green curves are the electron distribution shown in Figure 6e. We define the beam direction as the direction either parallel or antiparallel to \mathbf{B} where $\sum f_{\parallel}/f_{\perp}$ is largest for $E_e > 500$ eV. (c) Histogram of v_b/v_e estimated from the distributions associated with Langmuir waves.

In Figures 10a and 10b we plot f_{\parallel}/f_{\perp} for all averaged pitch-angle distributions associated with Langmuir waves in the beam direction and anti-aligned with the beam direction, respectively. For Langmuir waves there are 1855 snapshots with electron distributions. All

f_{\parallel}/f_{\perp} are plotted in gray, while the median f_{\parallel}/f_{\perp} as a function of E_e is plotted in red. We plot f_{\parallel}/f_{\perp} calculated from Figure 6e in green, which is characterized by $f_{\parallel}/f_{\perp} \gg 1$ for $2 \text{ keV} \lesssim E_e \lesssim 20 \text{ keV}$, with f_{\parallel}/f_{\perp} peaking at $E_e \approx 4 \text{ keV}$ (Figure 10a). In contrast, in the opposite direction to the beam f_{\parallel}/f_{\perp} does not show any clear enhancements over an extended E_e . In the beam direction there is a clear enhancement in the median of f_{\parallel}/f_{\perp} for $1 \text{ keV} \lesssim E_e \lesssim 10 \text{ keV}$. For comparison the median T_e associated with Langmuir waves is $T_e \approx 480 \text{ eV}$, so f_{\parallel}/f_{\perp} is enhanced at energies above the thermal energy of the electron distributions. In Figure 10b the median f_{\parallel}/f_{\perp} remains close to 1 for $E_e \gtrsim 1 \text{ keV}$, meaning the electron beam tends to be uni-directional. For $E_e \lesssim 1 \text{ keV}$ the median f_{\parallel}/f_{\perp} exceeds 1 in the direction anti-aligned with the beam, suggesting that the core electron population tends to have a bulk velocity in the opposite direction to the electron beam. These results show that there is typically an enhancement in the electron phase-space density either parallel or antiparallel to \mathbf{B} , suggestive of an electron beam, in association with the observed Langmuir waves.

We can estimate the beam speed for each electron distribution by finding the energies where f_{\parallel}/f_{\perp} peaks in the beam direction. For distributions where $f_{\parallel}/f_{\perp} > 10$ at some E_e we calculate v_b and compare with v_e . The results are shown in Figure 10c, which plots the histograms of v_b/v_e for all distributions with $f_{\parallel}/f_{\perp} > 10$. We find that 30 % of the distributions satisfy $f_{\parallel}/f_{\perp} > 10$. This further supports the result that clear electron beams are commonly associated with Langmuir waves. From Figure 10c we see that the electron beams typically have speeds several times higher than the background thermal speed with a median v_b/v_e of ≈ 3.2 . These beam speeds are consistent with generation of Langmuir or beam-mode waves.

We now perform the same statistical analysis for the UH waves. For UH waves the total number of snapshots with electron distributions is 519. In Figures 11a and Figures 11b we plot f_{\parallel}/f_{\perp} for all UH wave events in the beam direction and antiparallel to the beam direction. The green curves are the electron distribution in Figure 7e. For this example we find a significant enhancement in f_{\parallel}/f_{\perp} at $E_e \approx 1.4 \text{ keV}$, corresponding to the beam-like distribution. In the direction opposite to the beam there is a significant drop in f_{\parallel}/f_{\perp} centered around $E_e \approx 2.4 \text{ keV}$. The median f_{\parallel}/f_{\perp} shows an enhancement that peaks at $E_e \approx 1.2 \text{ keV}$, which is significantly smaller than for Langmuir waves. In the direction opposite to the beam the median f_{\parallel}/f_{\perp} exceeds 1 for $E_e \lesssim 2 \text{ keV}$, while for $E_e \gtrsim 2 \text{ keV}$ we find that $f_{\parallel}/f_{\perp} < 1$, suggestive of loss cone-like distributions.

We now calculate the thermal speeds of the electron beams and loss-cone distributions for UH waves. In Figure 11c we plot the histogram of v_b/v_e for the averaged electron distributions with beam features, i.e., for those with $f_{\parallel}/f_{\perp} > 10$ in the beam direction. We find that 9 % of the UH waves have clear beam features using the same definition as for Langmuir waves, which means that beam features are less likely to be seen in association with UH waves compared with Langmuir waves. Figure 11c shows that the beam energies tend to be less than or comparable to the background temperature, with median v_b/v_e of 0.9. Thus, the beams tend to be significantly slower than those typically associated with Langmuir waves.

In Figure 11d we plot the histogram of v_l/v_e , where v_l is the thermal speed of the loss cone and is calculated from E_e where f_{\parallel}/f_{\perp} is minimal and $f_{\parallel}/f_{\perp} < 0.1$ in the opposite direction to the beam. We find that 10 % of the distributions satisfy $f_{\parallel}/f_{\perp} < 0.1$, which is comparable to the number of beam distributions identified for UH waves. The loss cones tend to occur at superthermal speeds with median v_l/v_e of 2.3. We note that the small number of identified beams and loss cones is due to the high thresholds used to identify these features. For example, if we use $f_{\parallel}/f_{\perp} > 5$ and $f_{\parallel}/f_{\perp} < 0.2$ as thresholds we find that 30 % of distributions have beams or loss cones. Thus, we can conclude that beams and/or loss-cone-like distributions are commonly associated with UH waves.

Finally, we note that there are many distributions associated with the waves that do not show any clear evidence of instability. There are several possible reasons for this:

(1) For some of the wave events there are significant changes in the electron distributions while the snapshot is observed. In these cases unstable features may not be observed when the electron distributions are averaged.

(2) For many of the lobe-like distributions the densities are extremely small, so features associated with instability, such as weak beams or loss cones, may not be clearly measured because the counting statistics are very low.

(3) Some distributions are characterized by hot thermal electrons, with energies of several keV. In these cases the unstable part of the electron distribution may be at energies higher than those measured by FPI (above 30 keV).

(4) The waves may have been generated elsewhere and propagated into a region where unstable electron distributions are not observed.

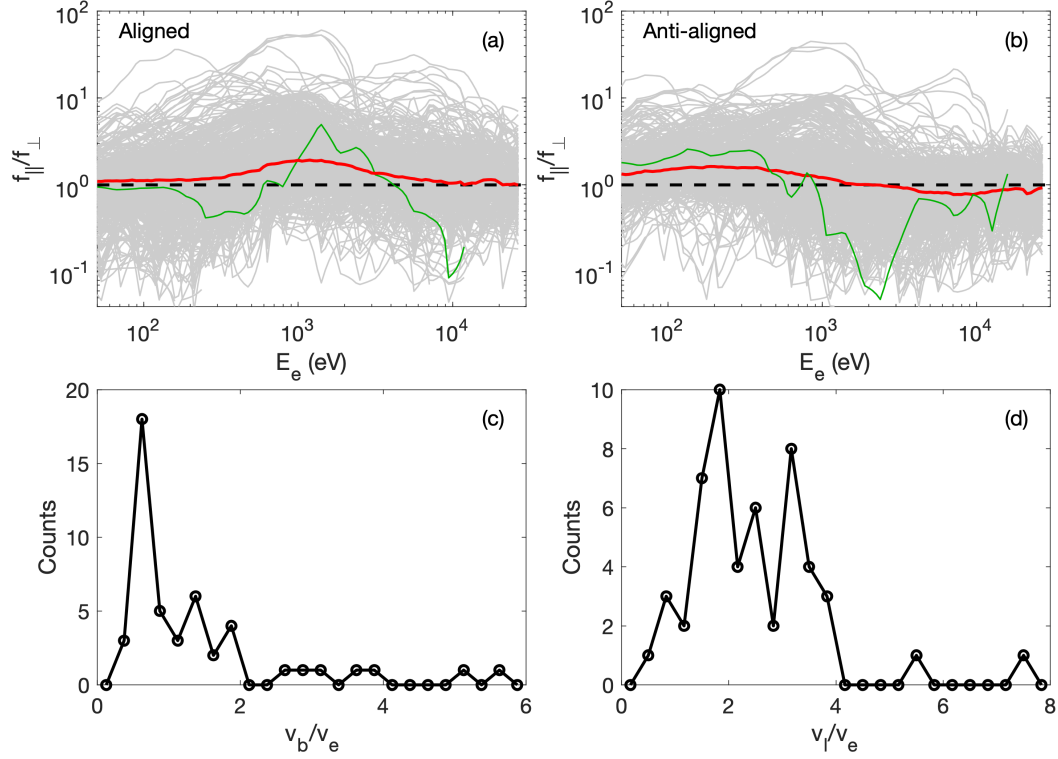


Figure 11. Statistical properties of the electron distributions associated with UH waves. (a) Plot of f_{\parallel}/f_{\perp} versus E_e in the electron beam direction for all electron distributions associated with UH waves (gray lines). (b) Plot of f_{\parallel}/f_{\perp} versus E_e for the direction anti-aligned with the beam for all electron distributions associated with UH waves. The red curves are the median f_{\parallel}/f_{\perp} of all distributions as a function of E_e and the green curves are the electron distribution shown in Figure 7e. (c) Histogram of v_b/v_e estimated from the distributions associated with UH waves. (d) Histogram of v_l/v_e estimated from the distributions associated with UH waves. We define v_l as the speed at which the loss-cone is deepest and satisfies $f_{\parallel}/f_{\perp} < 0.1$ in the direction antiparallel to the beam direction.

In summary, we find that the Langmuir waves are generated by the bump-on-tail instability. Evidence of field-aligned electron beams or beam remnants are commonly observed at the same time as the Langmuir waves. For the UH waves the source of instability is less clear. However, the electron distributions associated with UH waves are often characterized by drift of colder electrons in one direction, and a loss in hotter electrons in the opposite direction. We propose that a beam or a loss cone are likely responsible for the generation of most of the observed UH waves. Additionally, some of the UH waves are observed in the inner magnetosphere, where butterfly distributions are the likely source of instability, and near electron diffusion regions, where agyrotropic electron distributions are the source of instability.

5 The Role of Magnetic Reconnection

We now consider whether the observed Langmuir and UH waves, and their accompanying electron distributions, are associated with magnetic reconnection. We first consider two case studies and then look statistically at where the waves are found in relation to magnetic reconnection.

5.1 Case studies

To illustrate the relation of Langmuir and UH waves to ongoing magnetic reconnection we present two case studies in Figures 12 and 13, where reconnection and plasma frequency waves are observed. Figure 12 shows an event where Langmuir waves and a reconnection separatrix crossing are observed by MMS2 on 2017 July 06. Throughout the interval **B** remains approximately tailward (Figure 12a), meaning the spacecraft is southward of the central plasma sheet and reconnection X line. At the beginning of the interval MMS2 is in the tailward outflow region $V_{i,x} < 0$ (Figure 12b), where $V_{i,x}$ is the ion bulk speed in the GSM x direction. Between approximately 13:54:00 UT and 13:54:30 UT the ion flow is negligible and lobe-like plasma is observed, as indicated by the relatively low electron thermal speed v_e (Figure 12c). Between 13:54:36 UT and 13:56:40 UT we observe a large negative $V_{e,\parallel}$ adjacent to a tailward ion outflow. This electron flow is toward the reconnection X line and is identified as a separatrix region (Norgren et al., 2020). After this time MMS2 remains in the plasma sheet. The yellow-shaded regions indicate the times where Langmuir waves are observed; we do not observe any UH waves in this interval.

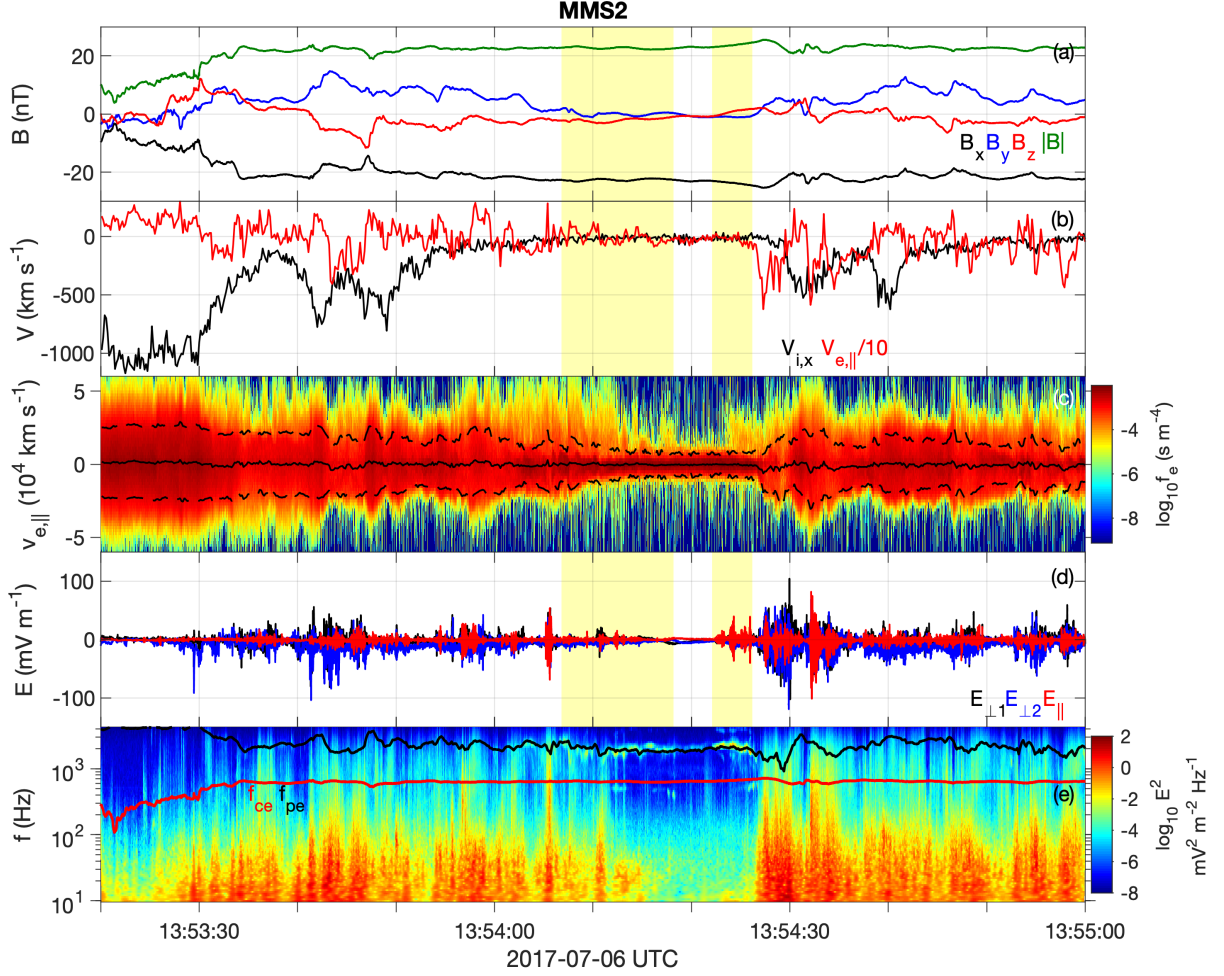


Figure 12. Example of Langmuir waves seen near the separatrix regions of magnetotail reconnection. (a) \mathbf{B} in GSM coordinates. (b) Ion bulk velocity in the x-direction $V_{i,x}$ (black) and electron velocity parallel to \mathbf{B} , $V_{e,||}$ (red). (c) One-dimensional reduced electron distribution along the \mathbf{B} direction. The solid and dashed black lines indicate $V_{e,||}$ and $V_{e,||} \pm v_e$, where v_e is the electron thermal speed. (d) and (e) Burst mode electric field in the field-aligned coordinate system and the associated frequency-time spectrogram. The black and red lines in (e) are f_{pe} and f_{ce} .

The Langmuir waves are seen at the local f_{pe} in Figure 12e, which plots the spectrogram of **E**. The Langmuir waves are only observed outside the outflow regions, where the plasma is lobe-like. When the Langmuir waves are observed there is an enhancement in f_e parallel to **B**, which forms the beam-like component of the electron distribution, in addition to the colder lobe electrons. For this event the beam electrons propagate away from the X line, based on the reconnection outflow direction. Since the Langmuir waves and electron beams are adjacent to the outflows and separatrix region, we propose that the electrons forming the beams are accelerated by magnetic reconnection along newly reconnected field lines, which are connected to the lobe plasma. These observations are consistent with the results in Viberg et al. (2013). In addition to the Langmuir waves we see broadband waves below f_{pe} , typically characterized by $E_{\perp} \gg E_{\parallel}$. The broadband waves occur in the reconnection outflow and separatrix region, and are typically lower amplitude when the Langmuir waves are observed.

In Figure 13 we show a reconnection event observed by MMS1 on 2017 July 09, where both Langmuir and UH waves are observed. Throughout most of the event $B_x > 0$ (Figure 13a), indicating that the spacecraft was northward of the central plasma sheet. An extended Earthward ion jet, $V_{i,x} > 0$, is observed between 17:16:00 UT and 17:18:05 UT (Figure 13b), indicating that the X line is tailward of the spacecraft. The ion jet initially peaked at 1000 km s⁻¹ then decreases to relatively small values where $|\mathbf{B}|$ is negligible. After this there is another increase in $V_{i,x}$. At 17:17:20 UT there is a dipolarization front, seen as the sharp increase in B_z . These features suggest that reconnection is unsteady over this interval.

Figures 13e and 13f show spectrograms of **E** and F_E . Near f_{pe} both Langmuir and UH waves are observed, as indicated by waves with both $F_E < 0.5$ and $F_E > 0.5$. In addition to the plasma frequency waves, we observe large-amplitude broadband waves primarily in the ion jets. Like the previous example, the Langmuir and UH waves are only observed outside the ion jet, where $V_{i,x}$ is negligible. We note that throughout most of the ion jet the density is too high to resolve f_{pe} in burst mode **E** data, although we do not observe any large-amplitude waves at f_{pe} from the hmfe snapshots within the ion jet.

Figure 13c shows the one-dimensional reduced electron distributions along **B**. In this event we only observe the lobe plasma at the end of the interval after 17:18:10 UT. At the beginning of the event the electrons have been heated compared with the lobe. The

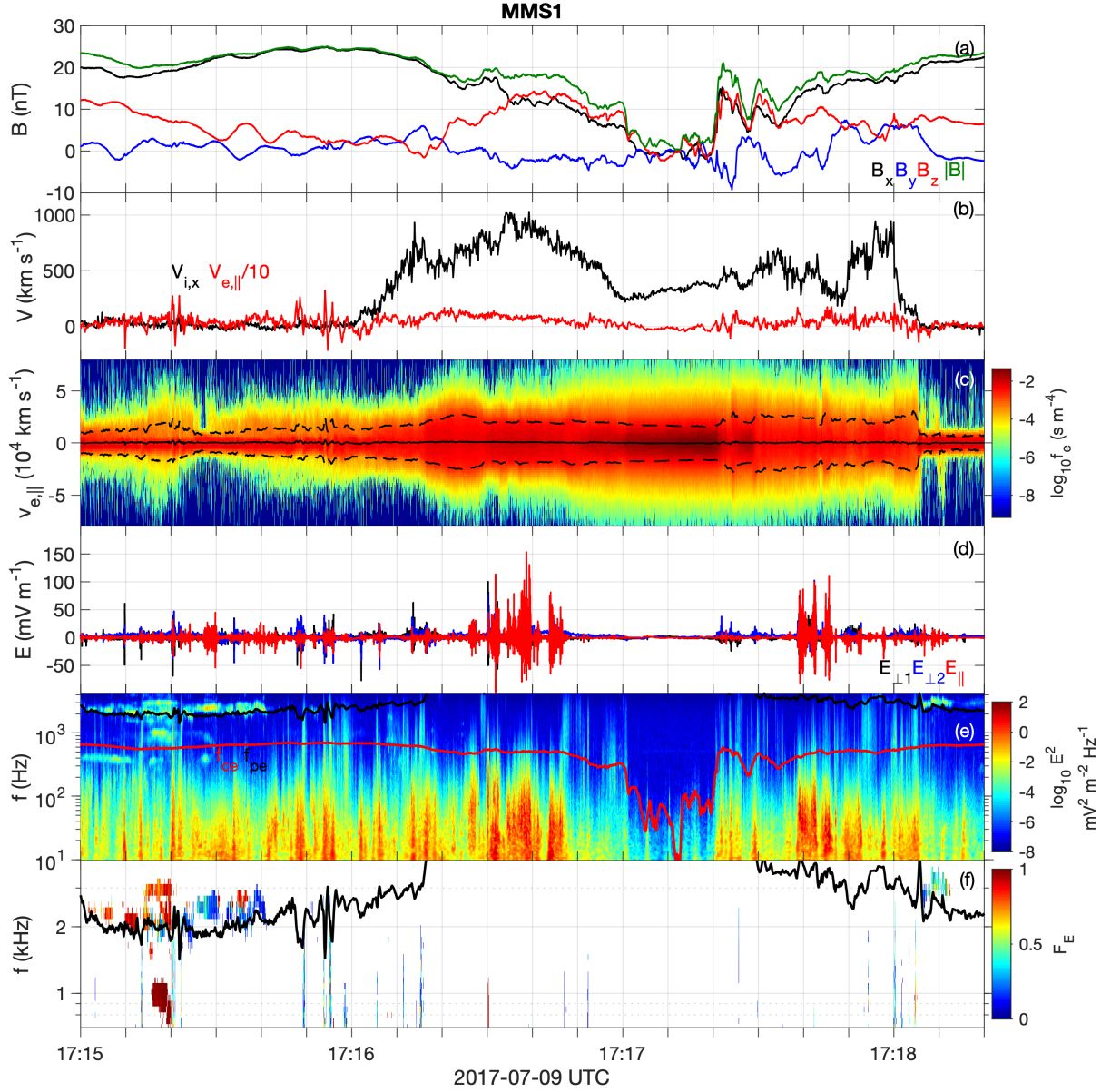


Figure 13. Example of Langmuir and UH waves associated with magnetotail reconnection. (a) \mathbf{B} in GSM coordinates. (b) Ion bulk velocity in the x-direction $V_{i,x}$ (black) and electron velocity parallel to \mathbf{B} , $V_{e,\parallel}$ (red). (c) One-dimensional reduced electron distribution along the \mathbf{B} direction. (d) and (e) Burst mode electric field in the field-aligned coordinate system and the associated frequency-time spectrogram. The black and red lines in (e) are f_{pe} and f_{ce} . (f) Spectrogram of F_E near f_{pe} (black line).

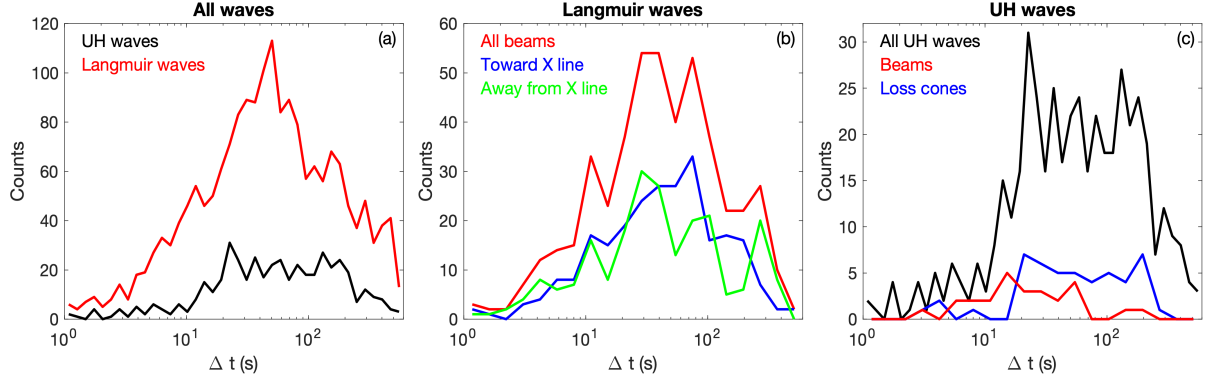
superthermal component of the distribution is primarily parallel to \mathbf{B} , away from the X line. By comparing Figure 13c with Figures 13e and 13f we see that the Langmuir and UH waves occur when there is a clear enhancement in f_e parallel to \mathbf{B} . The UH waves are observed where the plasma has been heated, i.e., v_e has increased compared with when Langmuir waves are observed. For UH waves the asymmetry between f_e parallel and antiparallel to \mathbf{B} is weaker compared with the nearby Langmuir waves. For the Langmuir waves observed around 17:18:10 UT the plasma is lobe-like with beam-like enhancements both parallel and antiparallel to \mathbf{B} . This suggests that beam-like electrons can propagate both toward and away from the local X line.

In these two examples Langmuir and UH waves are closely related to magnetotail reconnection. The waves are observed outside of, but close to, reconnection ion jets in the PSBL. This is consistent with statistical results in section 3, where the Langmuir and UH waves were most likely to occur for PSBL conditions. Likewise, the examples show that the waves occur in regions of the PSBL, where enhancements in f_e at supethermal energies either parallel or antiparallel to \mathbf{B} occur. These features are consistent with the beam-like electron distributions investigated in section 4.

5.2 Statistical results

We now investigate the relation of Langmuir and UH waves to reconnection statistically. We first consider whether the observed Langmuir and UH waves are found in close proximity to ion outflows from magnetic reconnection. For this study we define an ion outflow or jet as any region where $|V_{i,x}| > 200 \text{ km s}^{-1}$. For all snapshots we consider a 10 minute interval before and after the snapshot time to identify any nearby plasma jets. We use fast survey mode ion data, sampled every 4.5 s, to ensure there are no data gaps. We can then determine whether the observed waves are in ion jet regions or the time to the nearest jet. We can then calculate the fraction of Langmuir and UH waves observed within the reconnection outflow region and/or the time to the nearest ion outflow. For Langmuir waves we find that 97 % of all snapshots are within 10 minutes of a jet and only 14 % of all snapshots were found inside a jet. For UH waves 82 % of the snapshots are within 10 minutes of a jet and 9 % of snapshots were within a jet. Figure 14a shows the histograms of the times between the snapshot and nearest ion jet Δt for Langmuir and UH waves outside jet regions. We find that Δt peaks around 50 s with median Δt of 46 s for Langmuir waves, while for UH waves there is no clear peak but the median Δt is 54 s. We conclude that the waves are

678 closely associated with magnetic reconnection. We note that the burst mode selections in
 679 the magnetotail are strongly biased toward active regions where ion jets are observed, so
 680 it is unclear if Langmuir or UH waves can develop far from reconnection regions in the
 681 magnetotail.



682 **Figure 14.** Histograms of the times Δt between observed waves and ion jets. (a) Δt for all UH
 683 waves (black) and Langmuir waves (red). (b) Δt for all Langmuir waves where electron beams are
 684 observed (red), for beams toward the X line (blue), and for beams away from the X line (green).
 685 (c) Δt for all UH waves (black), for UH waves where beams are observed (red), and for UH waves
 686 where loss cones are observed (blue).

687 We now consider Langmuir waves where evidence of electron beams are observed using
 688 the criteria in section 4. Using the directions of \mathbf{B} and the nearest ion jet, we can infer
 689 whether the electron beams associated with the waves propagate toward or away from the
 690 local X line. We find that only 13 % of Langmuir waves with clear beam signatures occur in
 691 ion jets (Figure 15e provides an example of one of these electron distributions). In Figure
 692 14b we plot the histograms of Δt for all Langmuir waves where beams are identified, beams
 693 toward the X line, and beams away from the X line. We find that there is little clear
 694 difference in the histograms for beams toward or away from the X line. In both cases
 695 most electron beams are observed several tens of seconds from the nearest ion jet. At
 696 total of 545 events are found near ion jets. We observe comparable numbers if Langmuir
 697 wave events where the beams propagate toward the X line 48 % and away from the X line
 698 52 %. To explain this result, we first consider the number of Langmuir snapshots where
 699 the electron beams propagate Earthward or tailward. We find that 86 % of the beams
 700 propagate tailward, while only 14 % of the snapshots have Earthward beams. When we

divide the snapshots into events Earthward and tailward of the X line, we find that 21 % of the snapshots had Earthward beams when MMS was Earthward of the X line. When MMS was tailward of the X line only 4 % of the snapshots had Earthward beams. We note that 41 % of the Langmuir wave snapshots with electron beams were observed tailward of the local X line, so a statistically significant number of snapshots were found tailward of the X line. Therefore, electron beams associated with Langmuir waves are primarily tailward, regardless of whether the Langmuir waves are Earthward or tailward of the X line.

Our interpretation of these results is that most of the observed electron beams may not be generated by the local magnetic reconnection, but are likely electrons accelerated from the auroral regions along the magnetic field lines. The cause of these beams could be magnetic reconnection in the distant magnetotail, where the electrons are accelerated along the separatrices toward the distant magnetotail. The fact that Earthward electron beams are primarily observed Earthward of the local X line suggests that some of the observed electron beams are generated by local magnetic reconnection and propagate away from the X line. We expect these beams to occur in the outer separatrices where energetic electrons escape along newly reconnected field lines. Further inside the separatrix regions closer to the ion jets electrons tend to be accelerated toward the X line, although we rarely see Langmuir waves this close to the ion jets. Figure 15 shows a schematic of the electron beam directions in relation to the local reconnection X line.

We now investigate the electron distributions associated with UH waves, specifically the beams and loss cones identified in section 4, and their relation to magnetic reconnection. In Figure 14c we plot the time Δt between the UH waves and the nearest ion jet for all UH waves, beams associated with UH waves, and loss cones associated with UH waves. Although the total counts for beams and loss cones is relatively small, we find that Δt for beams tends to be smaller than for loss cones. The median Δt is 15 s for beams and 43 s for loss cones. These results suggest that the electron beams are closer to the separatrix regions of local reconnection compared to the loss cone distributions. We also note that the median Δt for beam associated with UH waves is significantly smaller than the median Δt for beams associated with Langmuir waves.

We now consider the directions of the beams associated with UH waves in relation to the local X line. In our dataset we find 33 snapshots of UH waves with electron beams near reconnection jets using the criteria in section 4. For these events 76 % had beams

propagating toward the X line, which is consistent with electrons accelerated on newly reconnected field lines. However, we note that 70 % of the events were observed Earthward of the X line, so it is unclear if the beams propagate toward the local X line or toward the distant magnetotail.

For the loss-cone distributions associated with UH we identify 52 snapshots near ion jets. We find that 94 % of the loss-cone distributions have a loss in electrons directed toward the X line. This is consistent with energetic electrons escaping on newly reconnected field lines. However, about 85 % of the events were observed Earthward of the X line and 83 % of the events had a loss in tailward propagating electrons. Thus, the loss in electrons is typically in the same direction as for beams associated with Langmuir and UH waves when loss-cone-like distributions are identified.

We conclude that the Langmuir and UH waves observed in the magnetotail are closely associated with magnetic reconnection. Most waves are observed near but outside of reconnection jets. For Langmuir waves the electron beams tend to propagate tailward, although a smaller number of beams are consistent with propagation away from the local magnetotail X line. These electron beam directions are illustrated in Figure 15. Figures 15a and 15b show examples of tailward and Earthward enhancements in f_e Earthward of the X line. Figure 15d shows a tailward beam observed tailward of the X-line. For UH the beams also tend to propagate tailward close to the X line, while for loss-cone-like distributions there tends to be a loss in tailward propagating electrons at superthermal speeds. However, for UH waves there are a relatively small number of clear beam or loss-cone distributions.

6 Conclusions

In this paper we have investigated the properties and occurrence of Langmuir and UH waves in Earth's magnetotail using the MMS spacecraft. The key results are:

1. Langmuir and UH waves are observed throughout the outer magnetosphere and near the magnetopause and in the magnetotail. Near the magnetopause UH waves are more commonly observed than Langmuir waves, while in the magnetotail Langmuir waves are more common than UH waves. The occurrence rate of plasma frequency waves is higher at the magnetopause, compared with in the magnetotail.
2. Langmuir and UH waves are most likely observed for lobe and PSBL plasma conditions, with occurrence rates of a few percent in the PSBL. The occurrence rate of

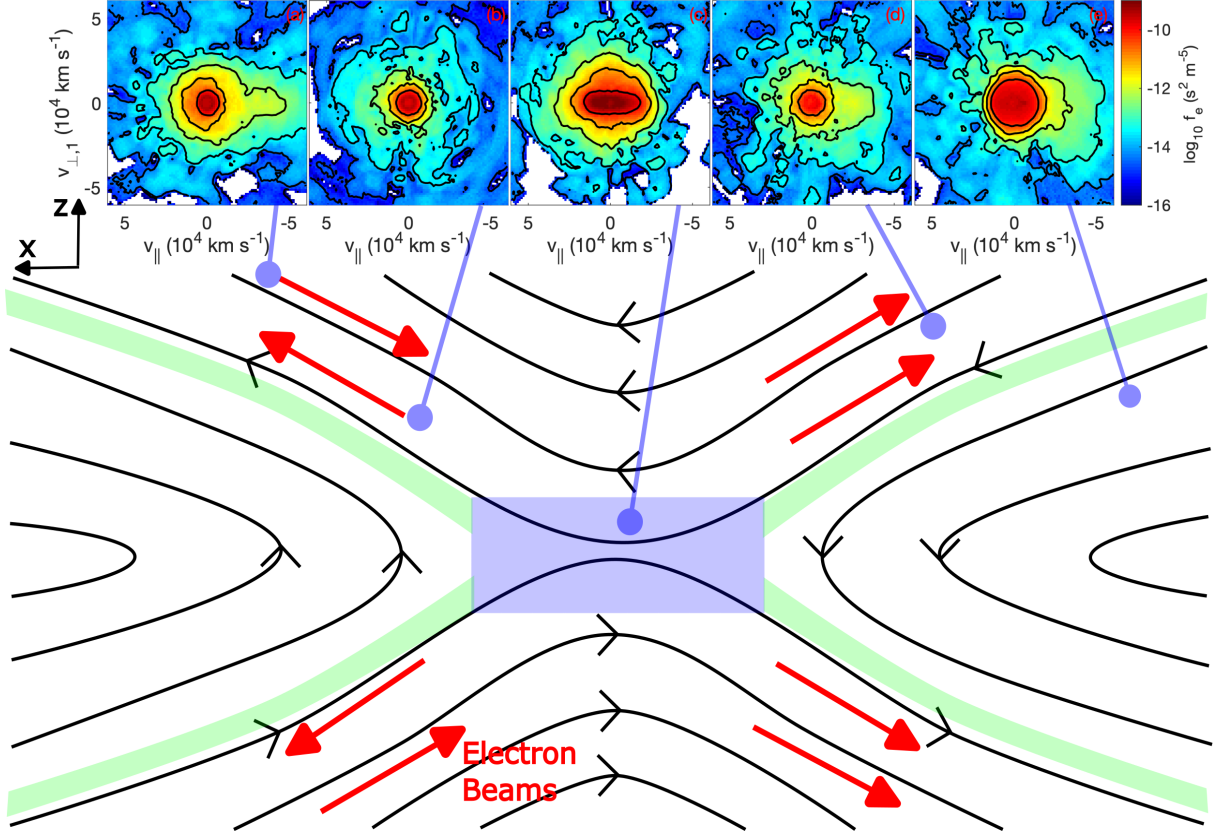


Figure 15. Schematic of magnetic reconnection in Earth's magnetotail in the GSM x-z plane. The black lines indicate the magnetic field lines. The blue and green shaded regions indicate the diffusion region and separatrix regions that bound the inflow and outflow plasmas, respectively. The red arrows outside the separatrices indicate the electron beam directions. Panels (a)–(e) show example electron distributions associated with Langmuir waves in the magnetotail. (a) and (b) Distributions with electron tailward and Earthward electron beams observed Earthward of the X line. (c) Distribution in the electron diffusion region. (d) Tailward beam observed tailward of the X line. (e) Tailward electron beam observed in the tailward ion outflow region.

772 plasma frequency waves is extremely small (a fraction of a percent) in the central
773 plasma sheet.

- 774 3. Langmuir waves are found to be generated by the bump-on-tail instability in the
775 PSBL. UH waves are primarily associated with broad electron beam populations
776 and/or loss-cone-like distributions, which are the likely sources of instability. Some
777 UH waves are associated with butterfly electron distributions in the magnetosphere
778 and agyrotropic electron distributions near electron diffusion regions.
- 779 4. The Langmuir and UH are typically observed close to but outside of ion jets associ-
780 ated with magnetotail reconnection. For Langmuir waves the electron beams tend to
781 propagate tailward regardless of whether the waves are observed Earthward or tail-
782 ward of the local X line. A smaller number of beams are consistent with propagation
783 away from the local X line. For UH waves the associated electron beams tend to
784 propagate tailward. For the loss-cone-like distributions there is typically a loss in
785 tailward electrons.

786 Open Research Section

787 The MMS data used in this study are available at [https://lasp.colorado.edu/mms/](https://lasp.colorado.edu/mms/sdc/public/data/)
788 [sdcp/public/data/](https://lasp.colorado.edu/mms/sdc/public/data/) in following the directories: `mms#/edp/brst/l2/hmfe/` for EDP hmfe
789 snapshot data, `mms#/edp/brst/l2/dce/` for EDP burst mode data, `mms#/fgm/brst/l2`
790 for FGM data, `mms#/fpi/brst/l2/des-moms` and `mms#/fpi/brst/l2/des-partmoms` for FPI
791 electron moments, `mms#/fpi/brst/l2/des-dist` for FPI electron distributions, and `mms#/fpi/fast/l2/dis-`
792 `moms` for FPI ion moments. Data analysis was performed using the `irfu-matlab` software
793 package.

794 Acknowledgments

795 We thank the entire MMS team for data access and support. This work was supported by
796 the Swedish National Space Board, grant 128/17.

797 References

- 798 Briand, C. (2015, April). Langmuir waves across the heliosphere. *Journal of Plasma Physics*,
799 81(2), 325810204. doi: 10.1017/S0022377815000112
- 800 Burch, J., Dokgo, K., Hwang, K., Torbert, R., Graham, D., Webster, J., ... Le Contel, O.
801 (2019). High-frequency wave generation in magnetotail reconnection: Linear disper-

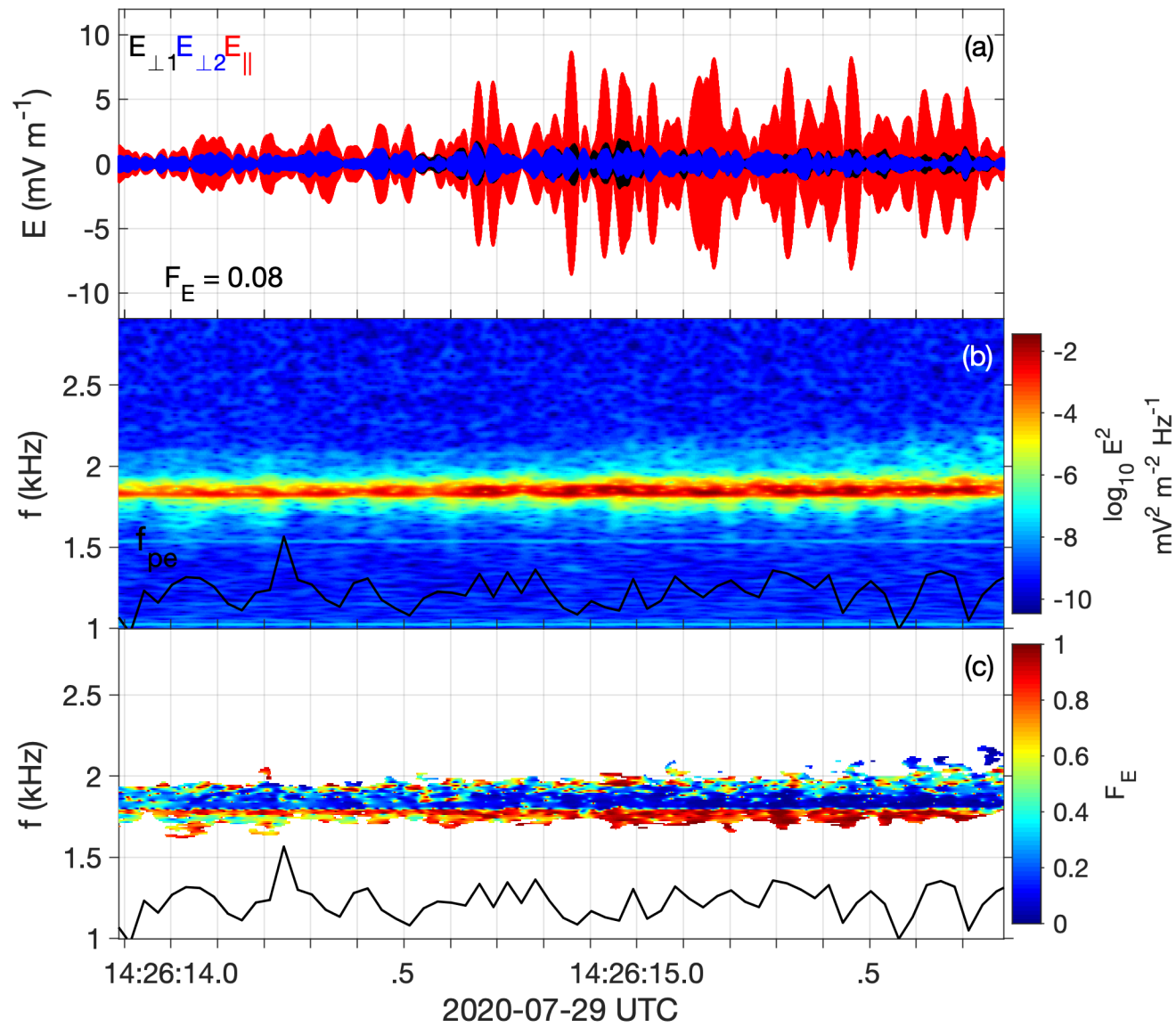
- sion analysis. *Geophysical Research Letters*, *46*(8), 4089-4097. doi: <https://doi.org/10.1029/2019GL082471>
- Cane, H. V., Stone, R. G., Fainberg, J., Steinberg, J. L., & Hoang, S. (1982). Type-II Solar Radio Events Observed in the Interplanetary Medium - Part One - General Characteristics. *Solar Physics*, *78*(1), 187-198. doi: 10.1007/BF00151153
- Dokgo, K., Hwang, K.-J., Burch, J. L., Choi, E., Yoon, P. H., Sibeck, D. G., & Graham, D. B. (2019). High-frequency wave generation in magnetotail reconnection: Nonlinear harmonics of upper hybrid waves. *Geophysical Research Letters*, *46*(14), 7873-7882. doi: <https://doi.org/10.1029/2019GL083361>
- Egedal, J., Fox, W., Katz, N., Porkolab, M., Oieroset, M., Lin, R. P., . . . Drake, J. F. (2008). Evidence and theory for trapped electrons in guide field magnetotail reconnection. *J. Geophys. Res.*, *113*, A12207. doi: 10.1029/2008JA013520
- Ergun, R. E., Tucker, S., Westfall, J., Goodrich, K. A., Malaspina, D. M., Summers, D., . . . Cully, C. M. (2016). The Axial Double Probe and Fields Signal Processing for the MMS Mission. *Space Sci. Rev.*, *199*, 167-188. doi: 10.1007/s11214-014-0115-x
- Etcheto, J., & Faucheux, M. (1984). Detailed study of electron plasma waves upstream of the earth's bow shock. *Journal of Geophysical Research: Space Physics*, *89*(A8), 6631-6653. doi: <https://doi.org/10.1029/JA089iA08p06631>
- Farrell, W. M., Desch, M. D., Kaiser, M. L., & Goetz, K. (2002). The dominance of electron plasma waves near a reconnection X-line region. *Geophys. Res. Lett.*, *29*, 1902. doi: 10.1029/2002GL014662
- Farrell, W. M., Desch, M. D., Ogilvie, K. W., Kaiser, M. L., & Goetz, K. (2003). The role of upper hybrid waves in magnetic reconnection. *Geophys. Res. Lett.*, *30*, 2259. doi: 10.1029/2003GL017549
- Filbert, P. C., & Kellogg, P. J. (1979). Electrostatic noise at the plasma frequency beyond the earth's bow shock. *Journal of Geophysical Research: Space Physics*, *84*(A4), 1369-1381. doi: <https://doi.org/10.1029/JA084iA04p01369>
- Fujimoto, K. (2014). Wave activities in separatrix regions of magnetic reconnection. *Geophys. Res. Lett.*, *41*, 2721. doi: 10.1002/2014GL059893
- Fuselier, S. A., Lewis, W. S., Schiff, C., Ergun, R., Burch, J. L., Petrinec, S. M., & Trattner, K. J. (2016, March). Magnetospheric Multiscale Science Mission Profile and Operations. *Space Science Reviews*, *199*(1-4), 77-103. doi: 10.1007/s11214-014-0087-x
- Gershman, D. J., Avakov, L. A., Boardsen, S. A., Dorelli, J. C., Gliese, U., Barrie, A. C.,

- 835 ... Pollock, C. J. (2017). Spacecraft and Instrument Photoelectrons Measured by
836 the Dual Electron Spectrometers on MMS. *Journal of Geophysical Research (Space*
837 *Physics)*, 122(A11), 11. doi: 10.1002/2017JA024518
- 838 Graham, D. B., Khotyaintsev, Y. V., Vaivads, A., Norgren, C., André, M., Webster, J. M.,
839 ... Russell, C. T. (2017). Instability of agyrotropic electron beams near the electron
840 diffusion region. *Phys. Rev. Lett.*, 119, 025101. doi: 10.1103/PhysRevLett.119.025101
- 841 Graham, D. B., Vaivads, A., Khotyaintsev, Y. V., André, M., Contel, O. L., Malaspina,
842 D. M., ... Torbert, R. B. (2018). Large-amplitude high-frequency waves at Earth's
843 magnetopause. *J. Geophys. Res.*, 123. doi: 10.1002/2017JA025034
- 844 Haaland, S., Kronberg, E. A., Daly, P. W., Fränz, M., Degener, L., Georgescu, E., &
845 Dandouras, I. (2010). Spectral characteristics of protons in the earth's plasmashet:
846 statistical results from cluster cis and rapid. *Annales Geophysicae*, 28(8), 1483–1498.
847 doi: 10.5194/angeo-28-1483-2010
- 848 Kurth, W. S., Craven, J. D., Frank, L. A., & Gurnett, D. A. (1979). Intense electrostatic
849 waves near the upper hybrid resonance frequency. *Journal of Geophysical Research:*
850 *Space Physics*, 84(A8), 4145-4164. doi: <https://doi.org/10.1029/JA084iA08p04145>
- 851 Kurth, W. S., Gurnett, D. A., & Anderson, R. R. (1981). Escaping nonthermal continuum
852 radiation. *Journal of Geophysical Research: Space Physics*, 86(A7), 5519-5531. doi:
853 <https://doi.org/10.1029/JA086iA07p05519>
- 854 Li, W.-Y., Khotyaintsev, Y. V., Tang, B.-B., Graham, D. B., Norgren, C., Vaivads, A.,
855 ... Wang, C. (2021). Upper-hybrid waves driven by meandering electrons around
856 magnetic reconnection x line. *Geophysical Research Letters*, 48(16), e2021GL093164.
857 doi: <https://doi.org/10.1029/2021GL093164>
- 858 Lin, R. P., Potter, D. W., Gurnett, D. A., & Scarf, F. L. (1981, December). Energetic elec-
859 trons and plasma waves associated with a solar type III radio burst. *The Astrophysical*
860 *Journal*, 251, 364-373. doi: 10.1086/159471
- 861 Lindqvist, P.-A., Olsson, G., Torbert, R. B., King, B., Granoff, M., Rau, D., ... Tucker, S.
862 (2016). The Spin-Plane Double Probe Electric Field Instrument for MMS. *Space Sci.*
863 *Rev.*, 199, 137-165. doi: 10.1007/s11214-014-0116-9
- 864 McFadden, J. P., Carlson, C. W., & Boehm, M. H. (1986). High-frequency waves generated
865 by auroral electrons. *Journal of Geophysical Research: Space Physics*, 91(A11), 12079-
866 12088. doi: <https://doi.org/10.1029/JA091iA11p12079>
- 867 Norgren, C., Hesse, M., Graham, D. B., Khotyaintsev, Y. V., Tenfjord, P., Vaivads, A.,

- 868 ... Burch, J. L. (2020). Electron acceleration and thermalization at magnetotail
869 separatrixes. *Journal of Geophysical Research: Space Physics*, *125*(4), e2019JA027440.
870 doi: <https://doi.org/10.1029/2019JA027440>
- 871 Pollock, C., Moore, T., Jacques, A., Burch, J., Gliese, U., Saito, Y., ... Zeuch, M. (2016).
872 Fast Plasma Investigation for Magnetospheric Multiscale. *Space Sci. Rev.*, *199*, 331-
873 406. doi: 10.1007/s11214-016-0245-4
- 874 Rönmark, K. (1982). WHAMP – Waves in homogeneous, anisotropic, multicomponent
875 plasmas. *technical report, Kiruna Geophys. Inst., Kiruna, Sweden.*
- 876 Russell, C. T., Anderson, B. J., Baumjohann, W., Bromund, K. R., Dearborn, D., Fischer,
877 D., ... Richter, I. (2016). The magnetospheric multiscale magnetometers. *Space Sci.*
878 *Rev.*, *199*, 189-256. doi: 10.1007/s11214-014-0057-3
- 879 Scarf, F. L., Fredricks, R. W., Frank, L. A., & Neugebauer, M. (1971). Nonthermal electrons
880 and high-frequency waves in the upstream solar wind, 1. observations. *J. Geophys. Res.*,
881 *76*(22), 5162–5171. doi: 10.1029/JA076i022p05162
- 882 Tataronis, J. A., & Crawford, F. W. (1970). Cyclotron harmonic wave propagation and
883 instabilities: I. Perpendicular propagation. *Journal of Plasma Physics*, *4*, 231-248.
884 doi: 10.1017/S0022377800004979
- 885 Viberg, H., Khotyaintsev, Y. V., Vaivads, A., André, M., & Pickett, J. S. (2013). Mapping
886 HF waves in the reconnection diffusion region. *Geophys. Res. Lett.*, *40*, 1032. doi:
887 10.1002/grl.50227
- 888 Winglee, R. M., & Dulk, G. A. (1986). The electron-cyclotron maser instability as a source
889 of plasma radiation. *Astrophys. J.*, *307*, 808-819. doi: 10.1086/164467
- 890 Wong, H. K., Menietti, J. D., Lin, C. S., & Burch, J. L. (1988). Generation of electron conical
891 distributions by upper hybrid waves in the earth's polar region. *Journal of Geophysical*
892 *Research: Space Physics*, *93*, 10025–10028. doi: 10.1029/JA093iA09p10025

Figure 1.

MMS2



MMS1

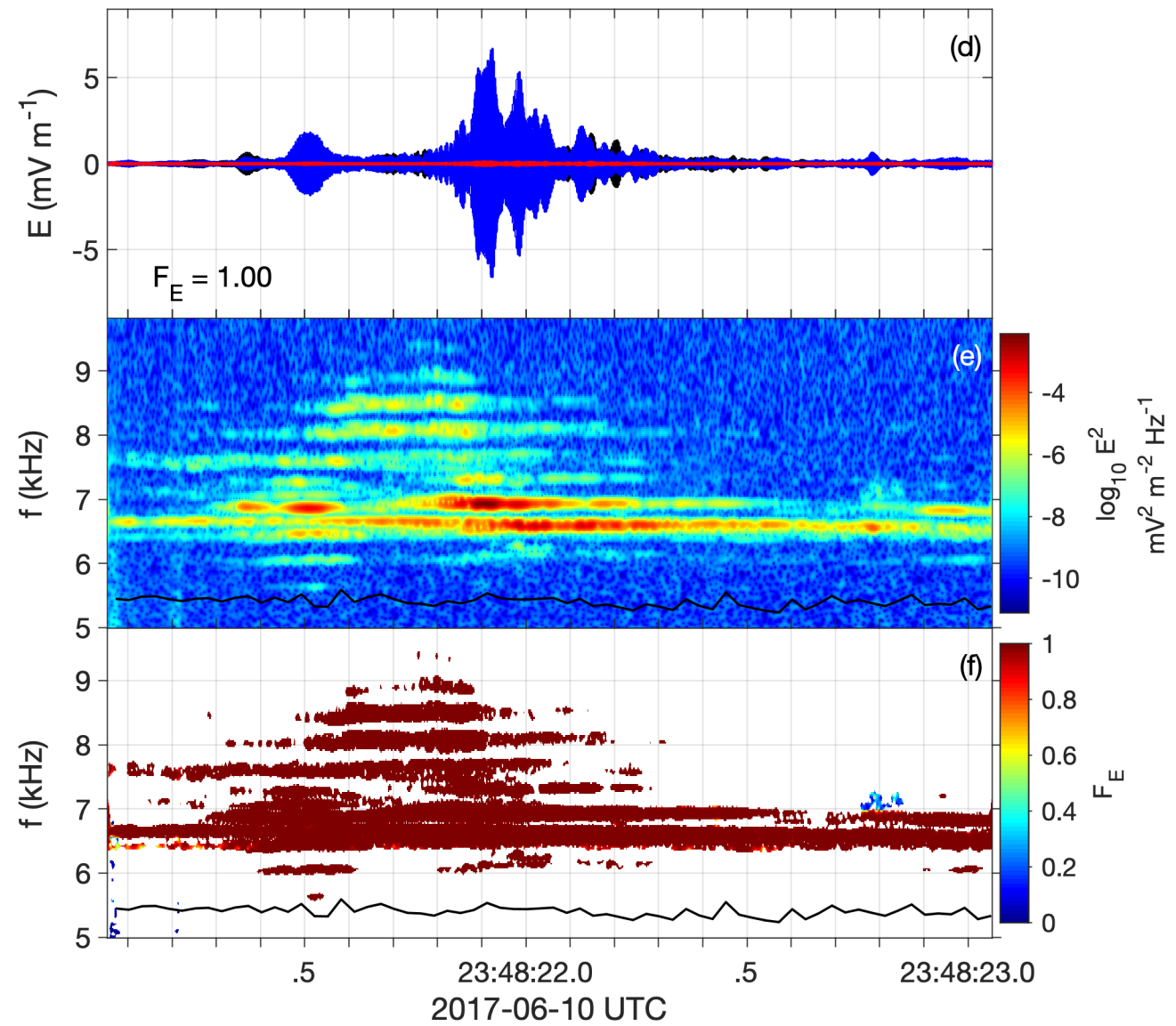


Figure 2.

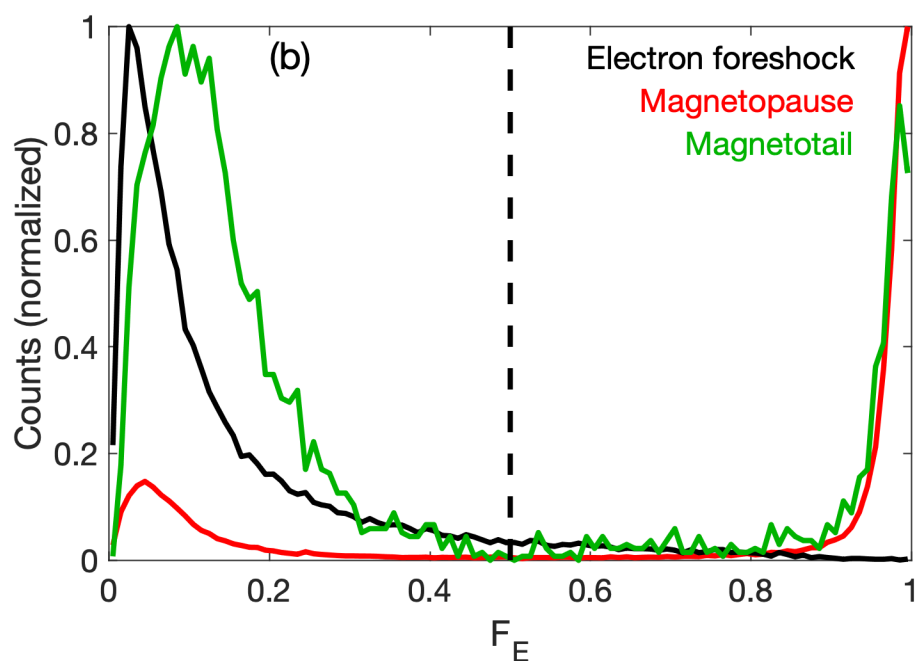
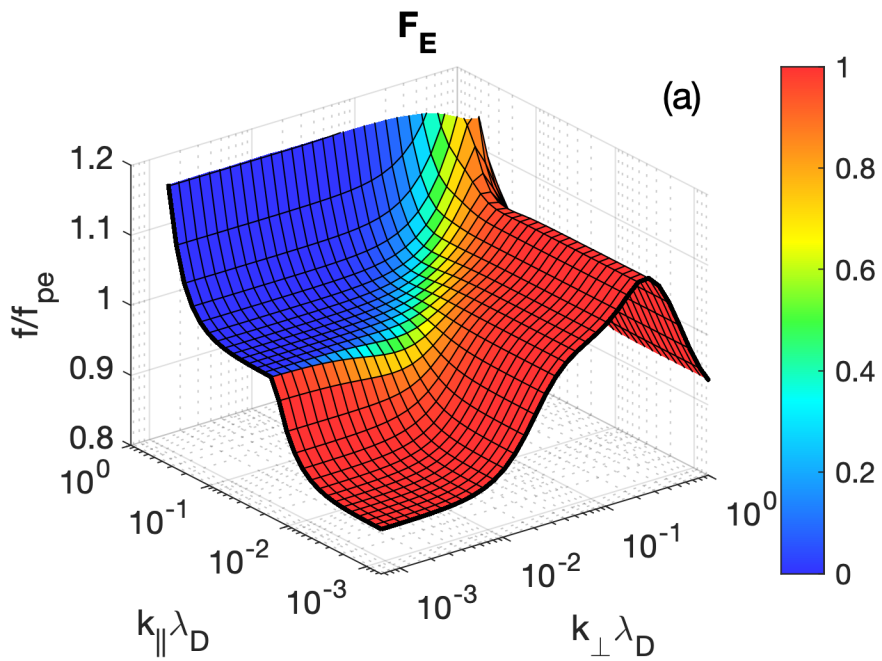


Figure 3.

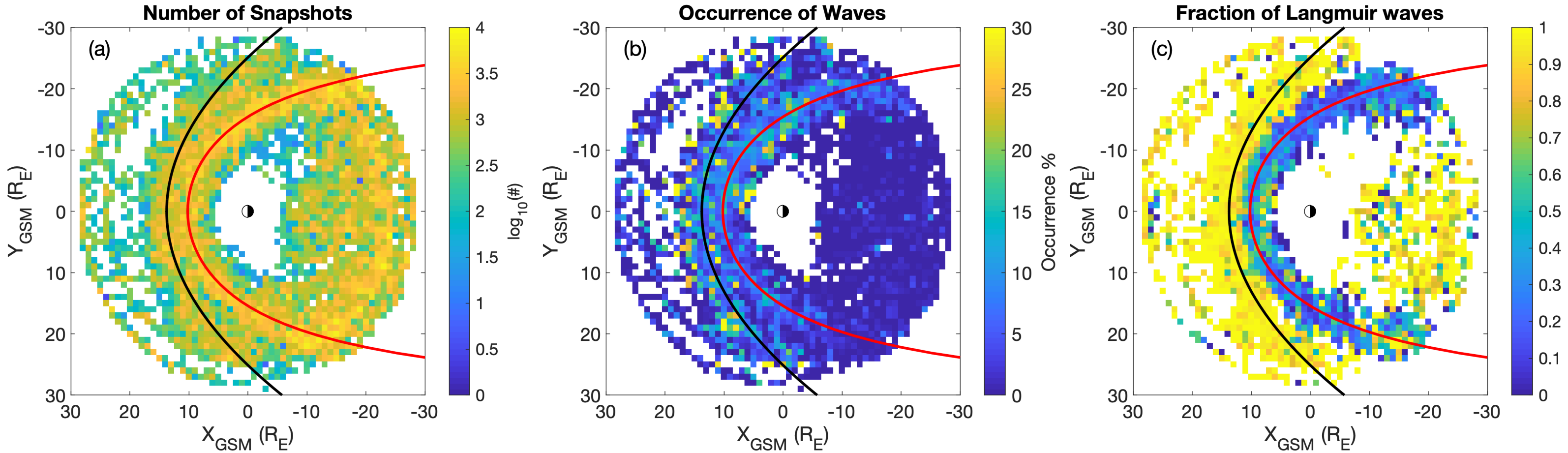


Figure 4.

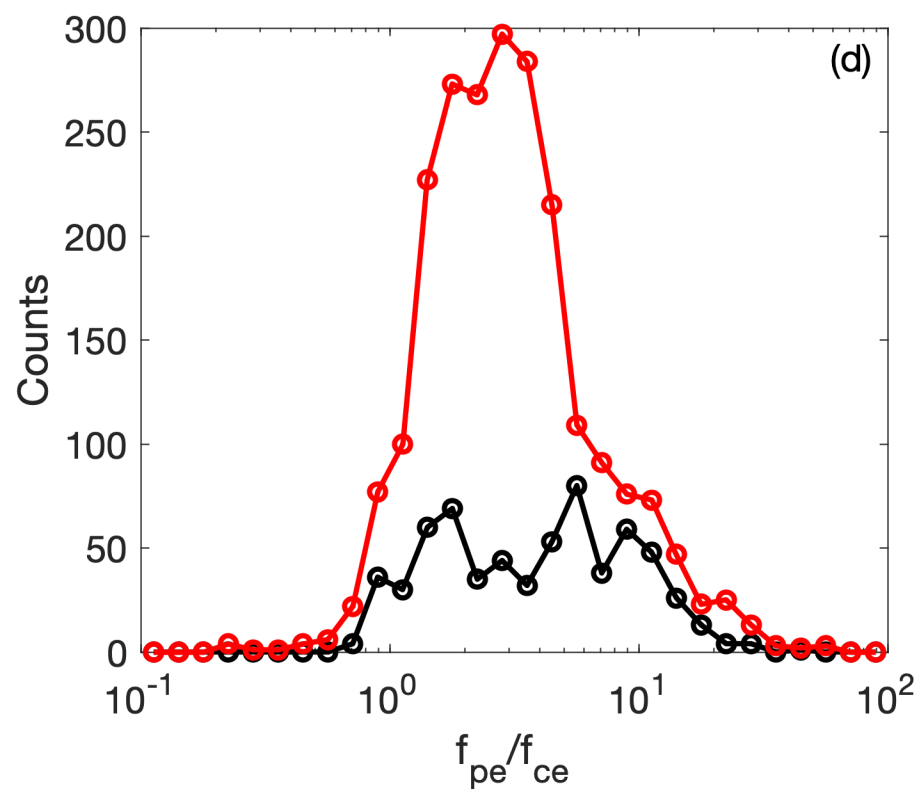
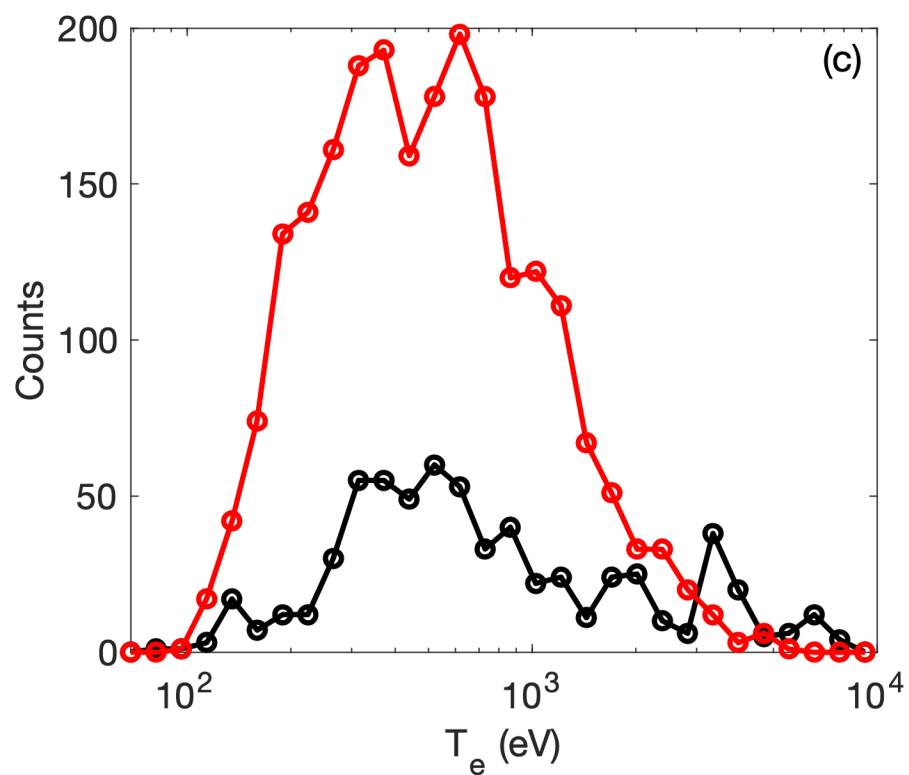
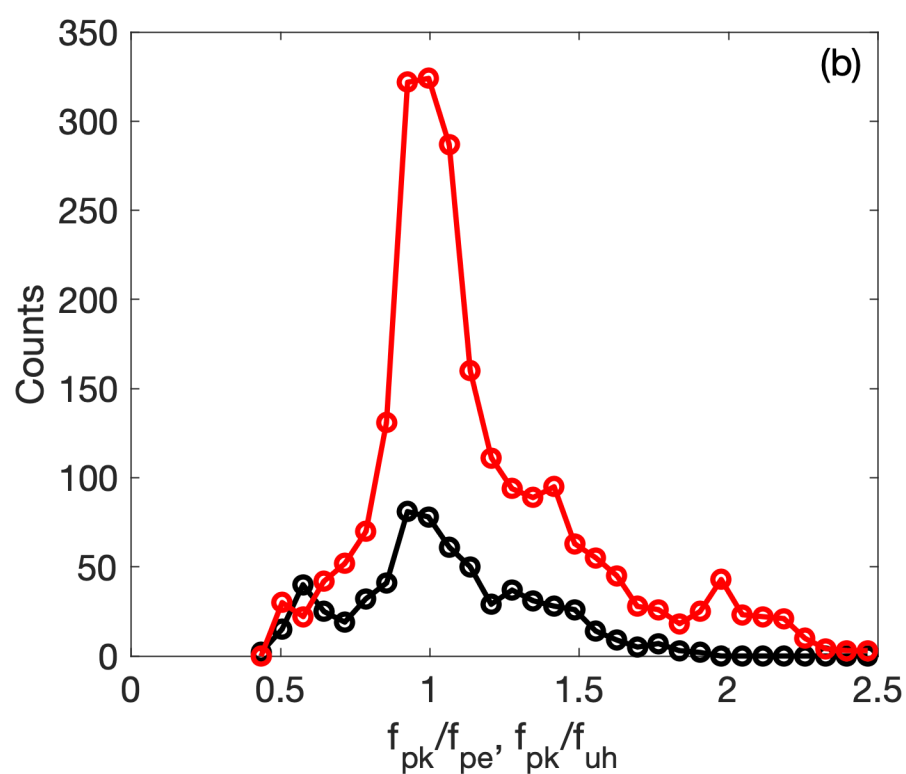
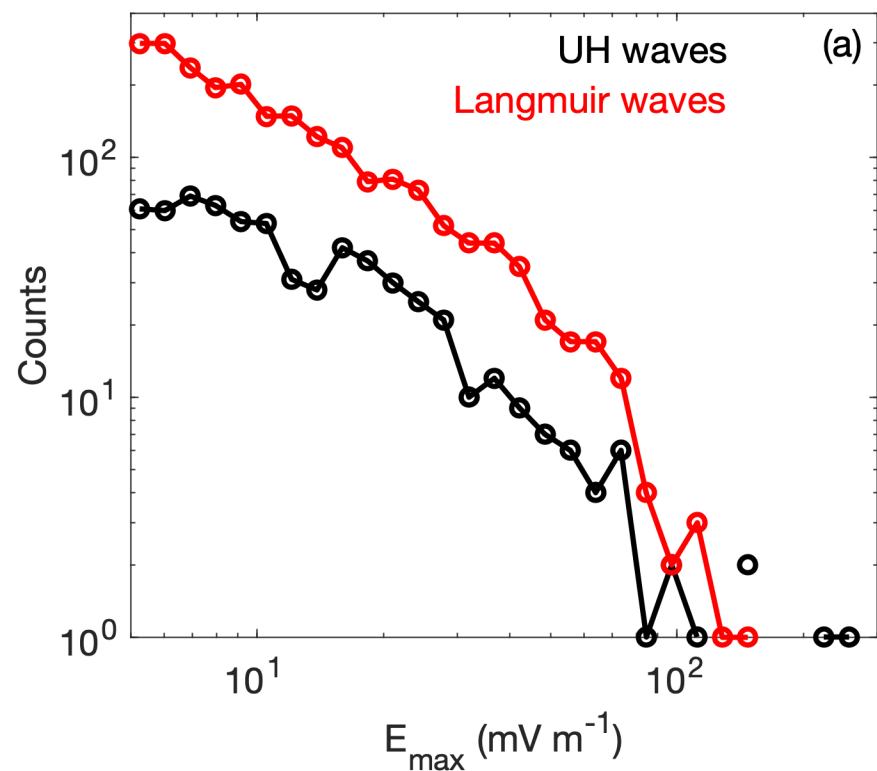


Figure 5.

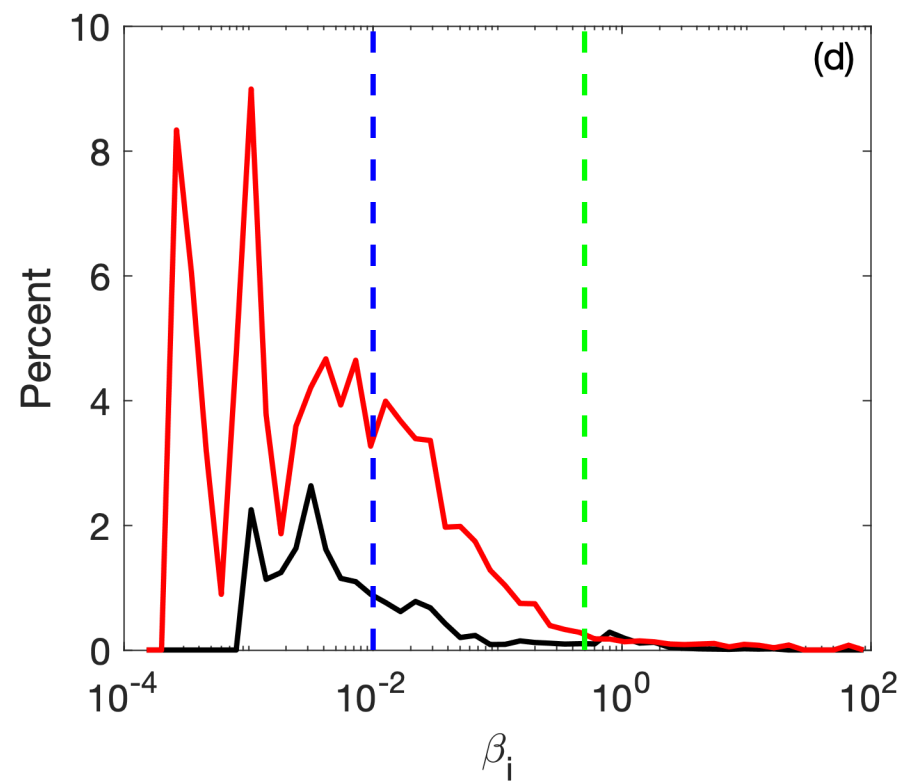
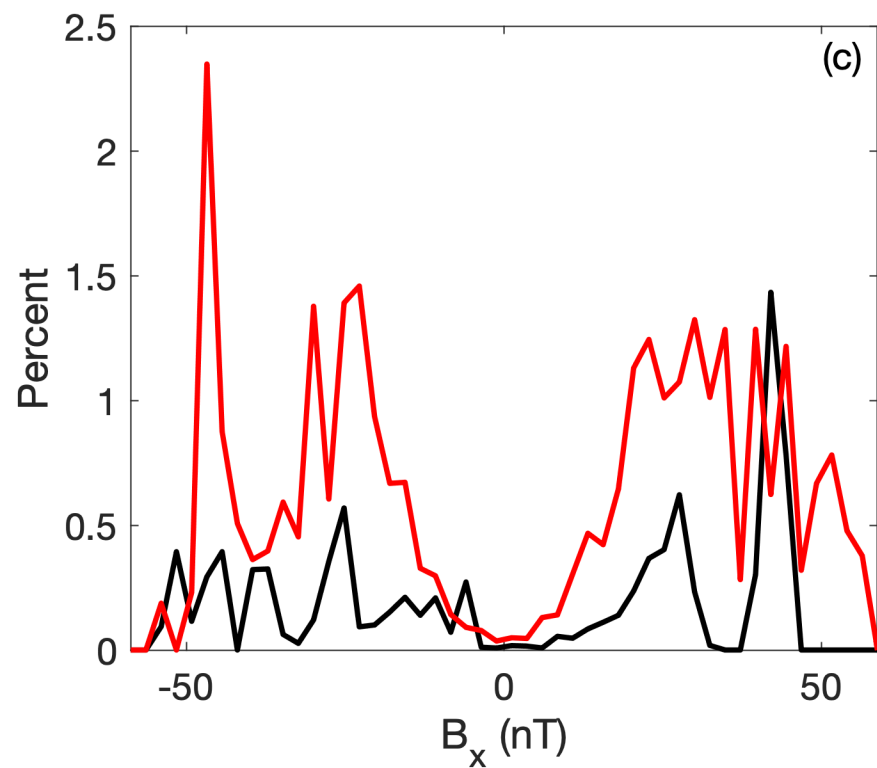
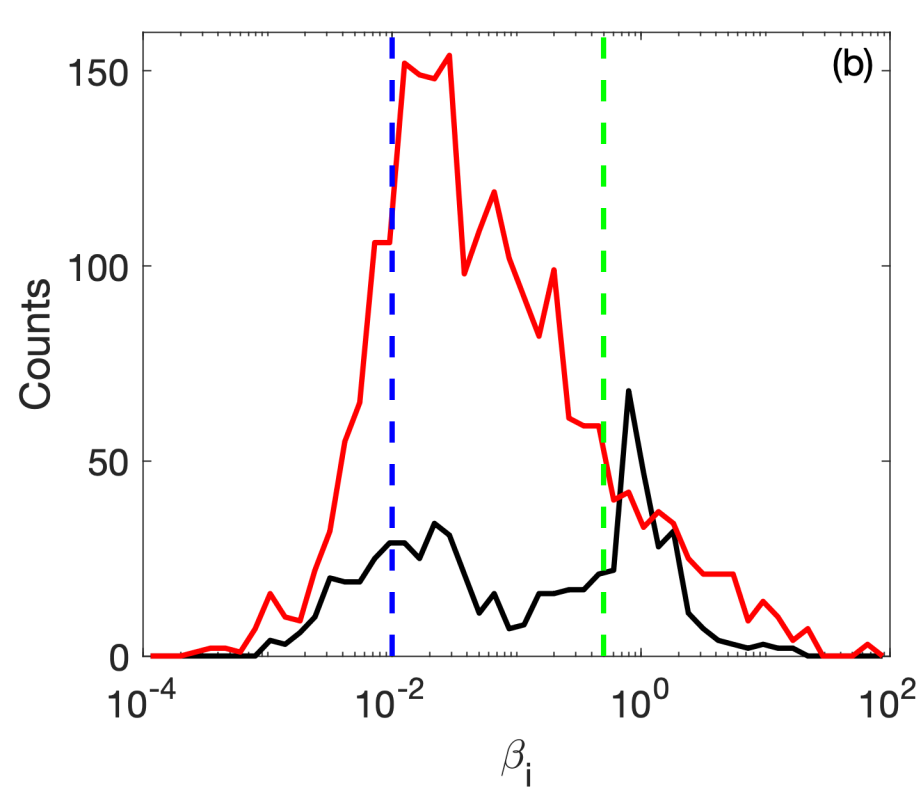
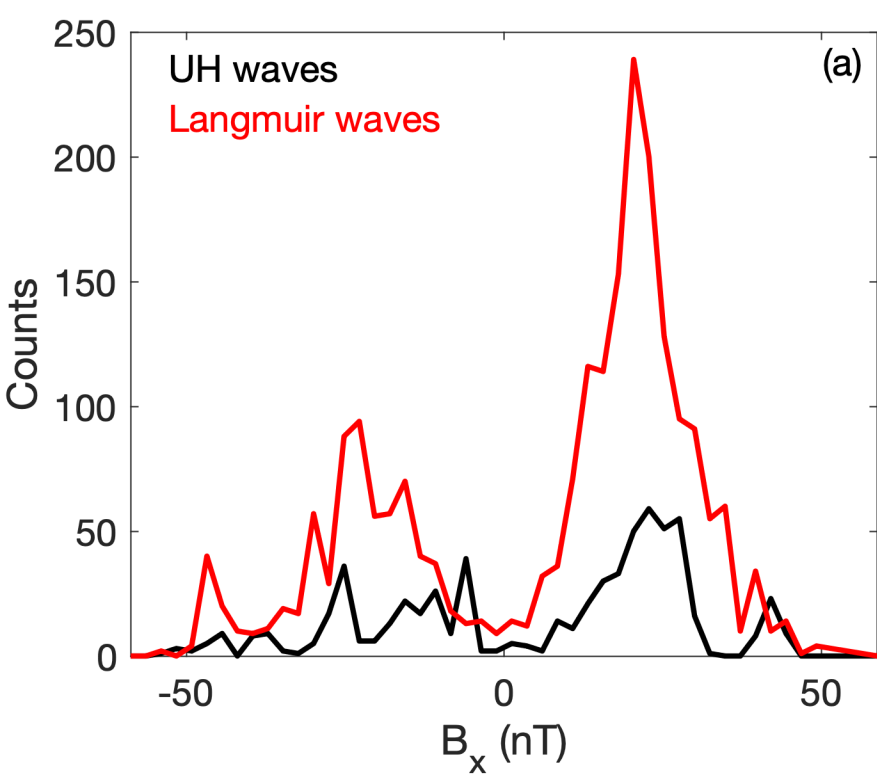


Figure 6.

MMS1: Langmuir Wave

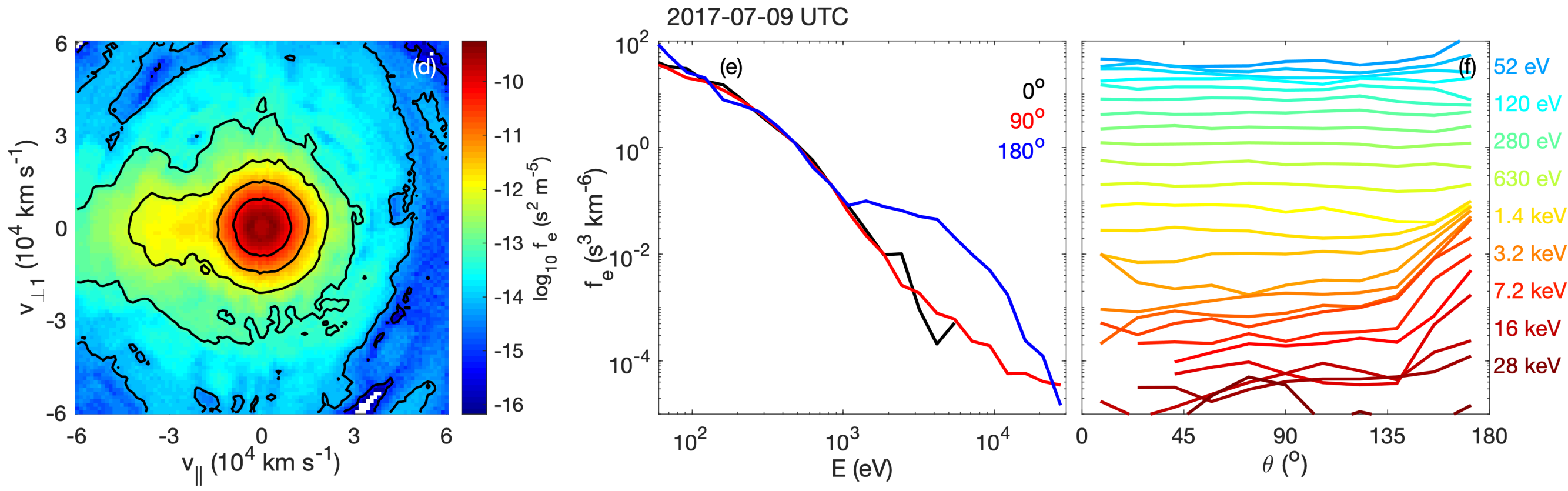
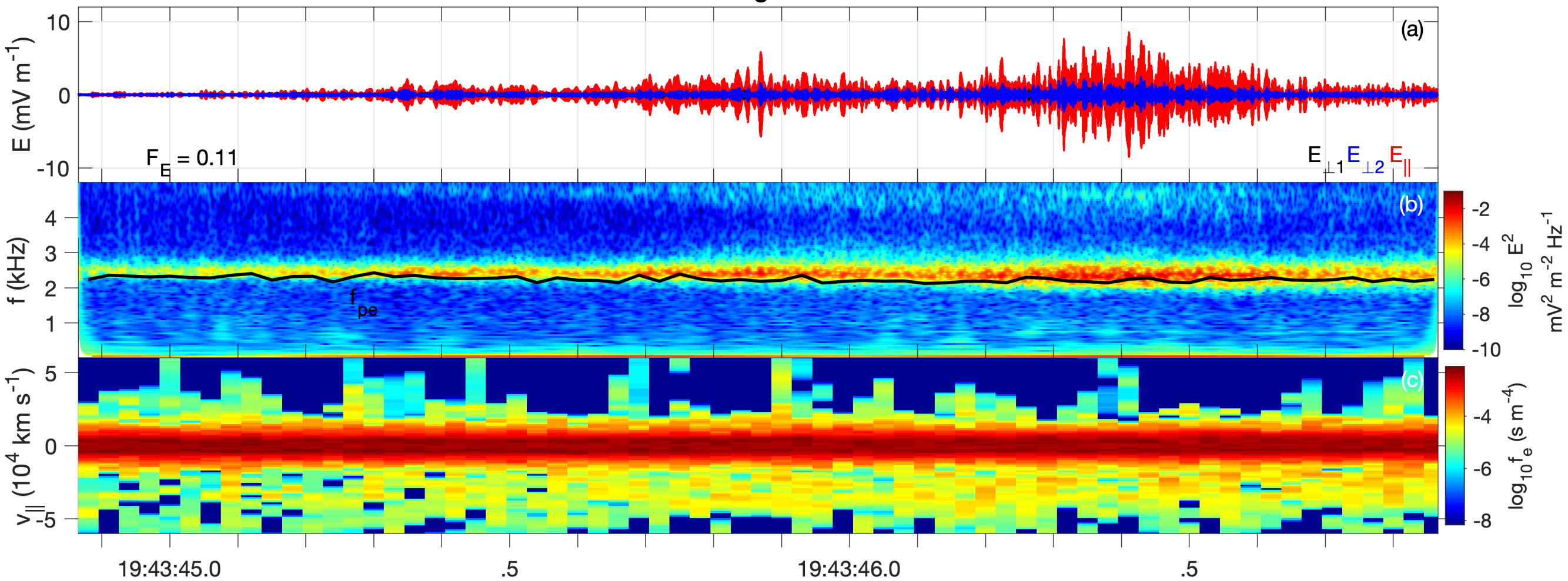


Figure 7.

MMS1: Upper Hybrid Wave

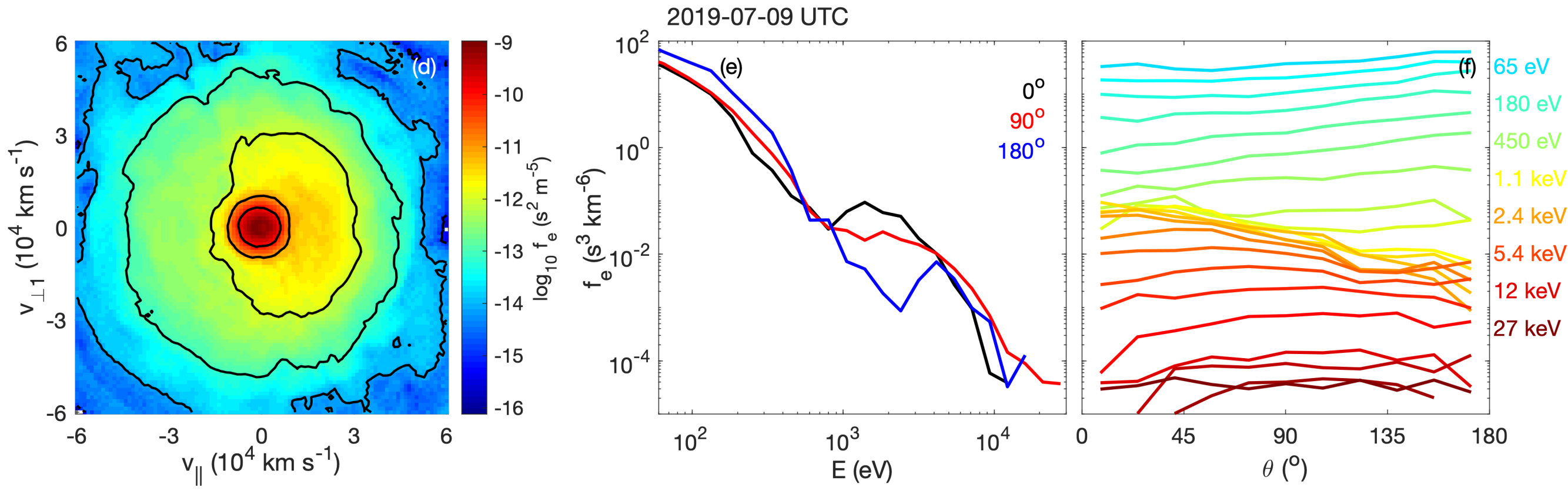
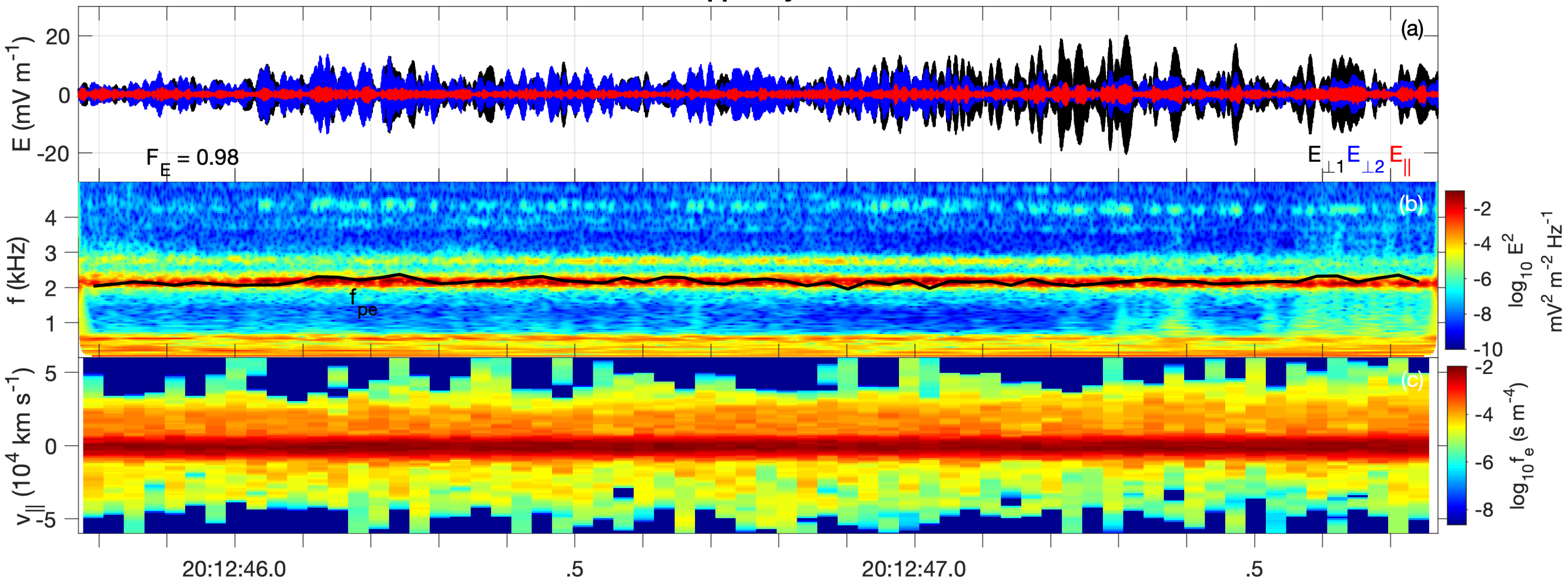


Figure 8.

MMS2

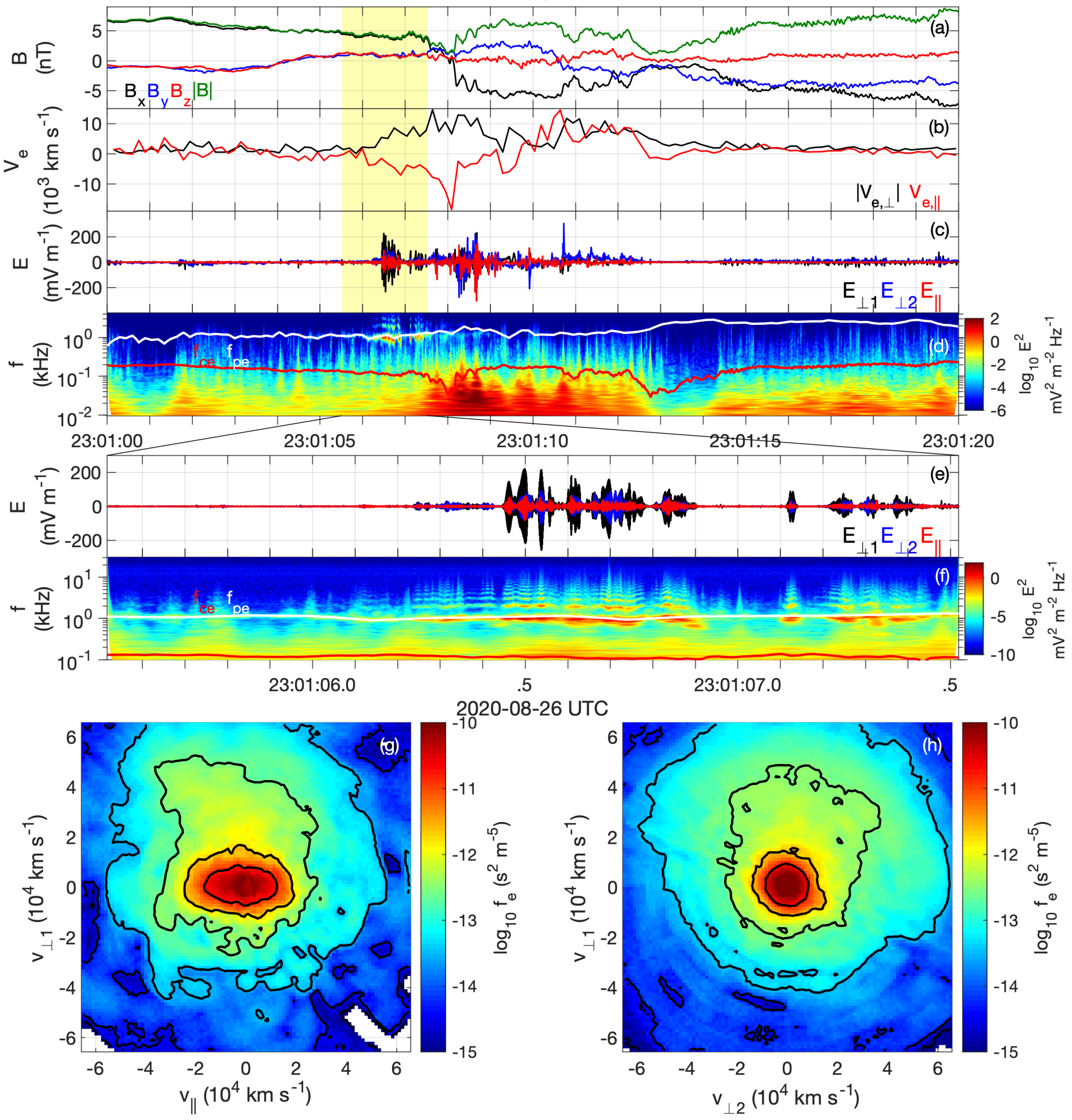


Figure 9.

MMS1

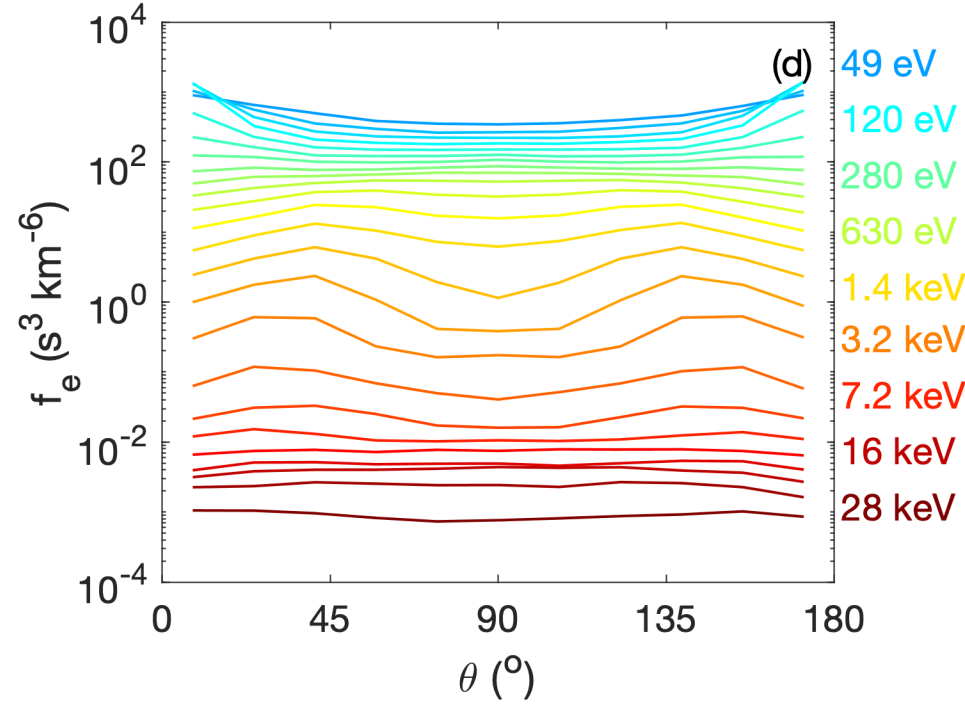
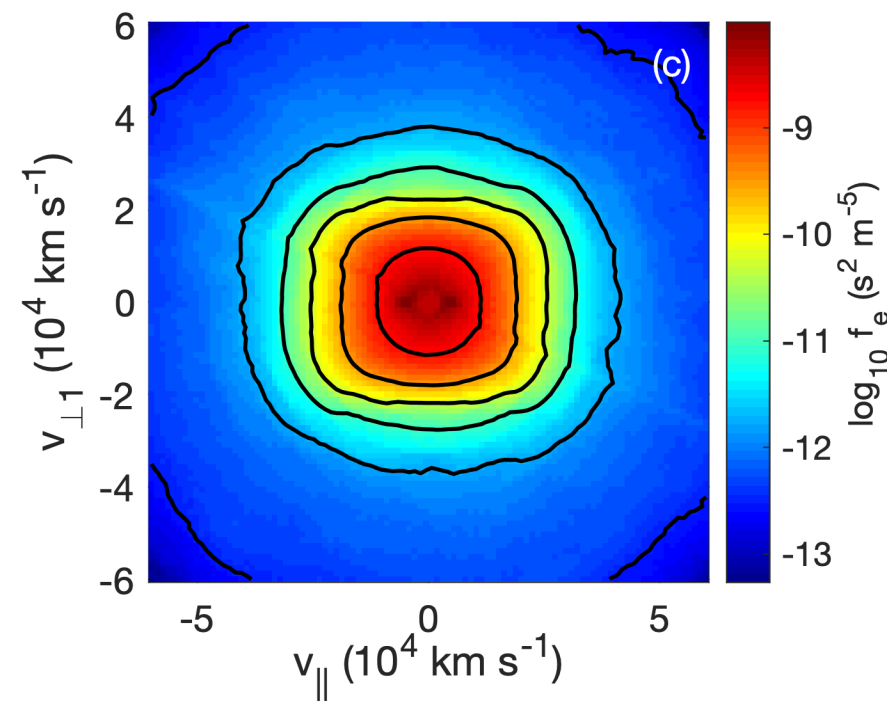
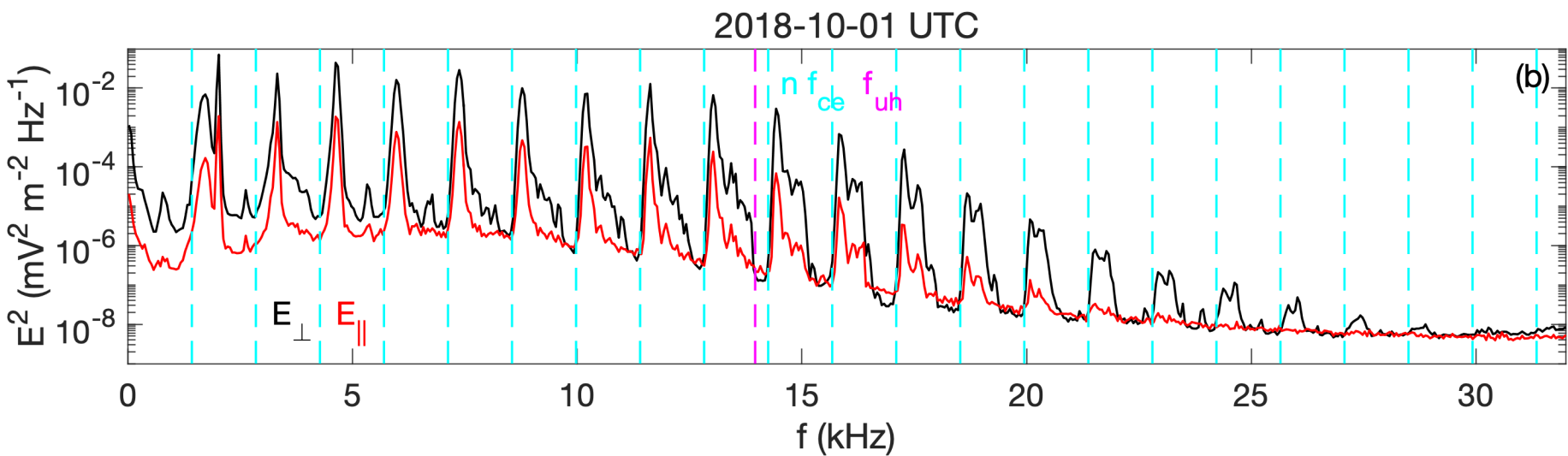
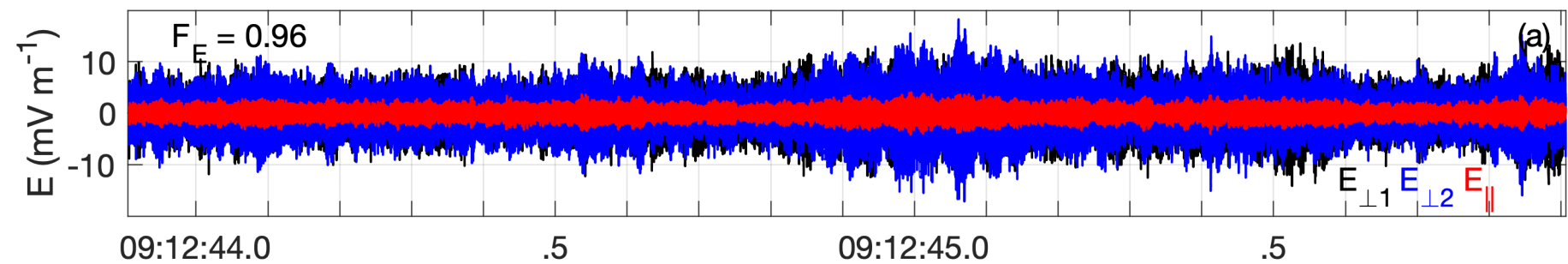


Figure 10.

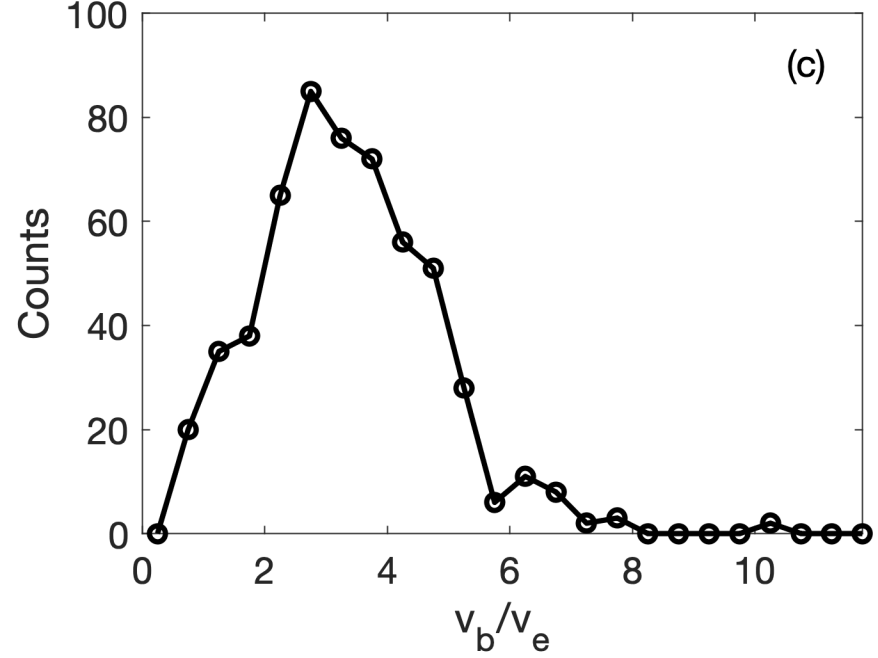
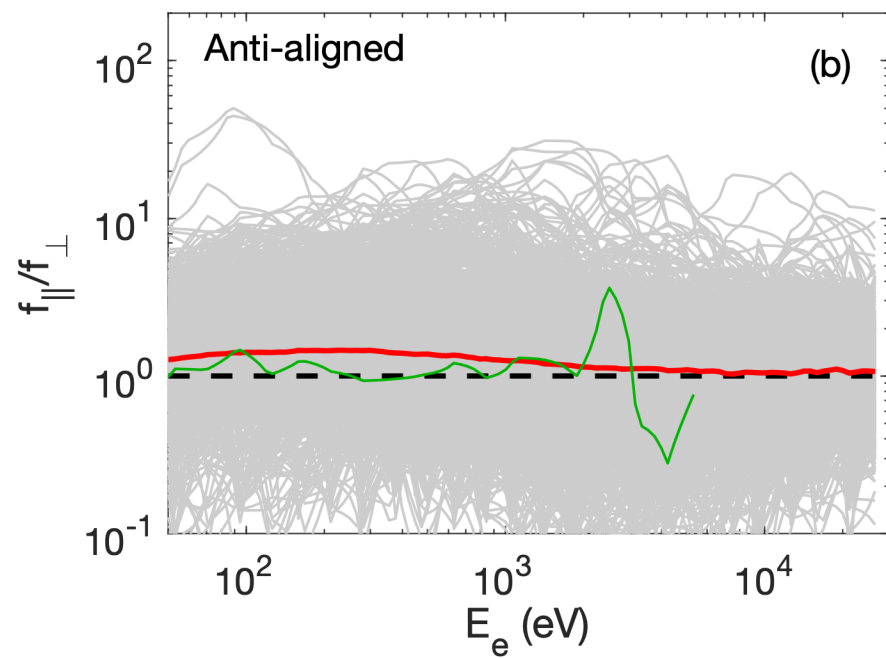
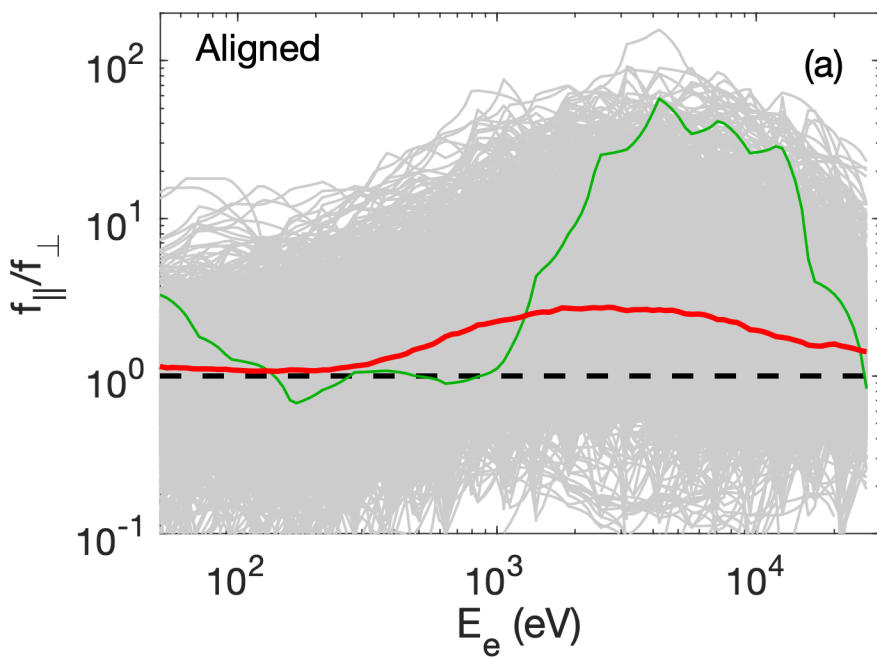


Figure 11.

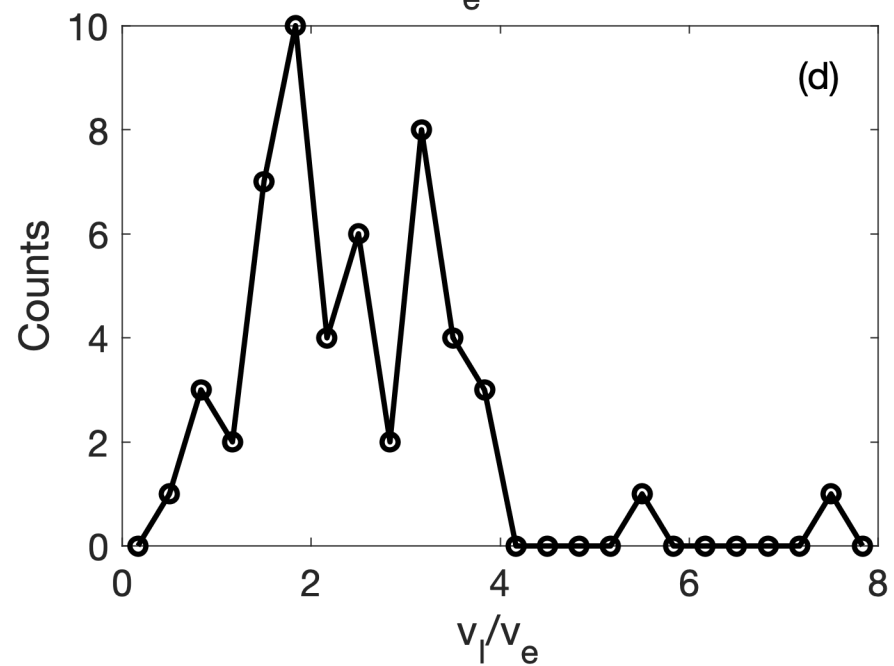
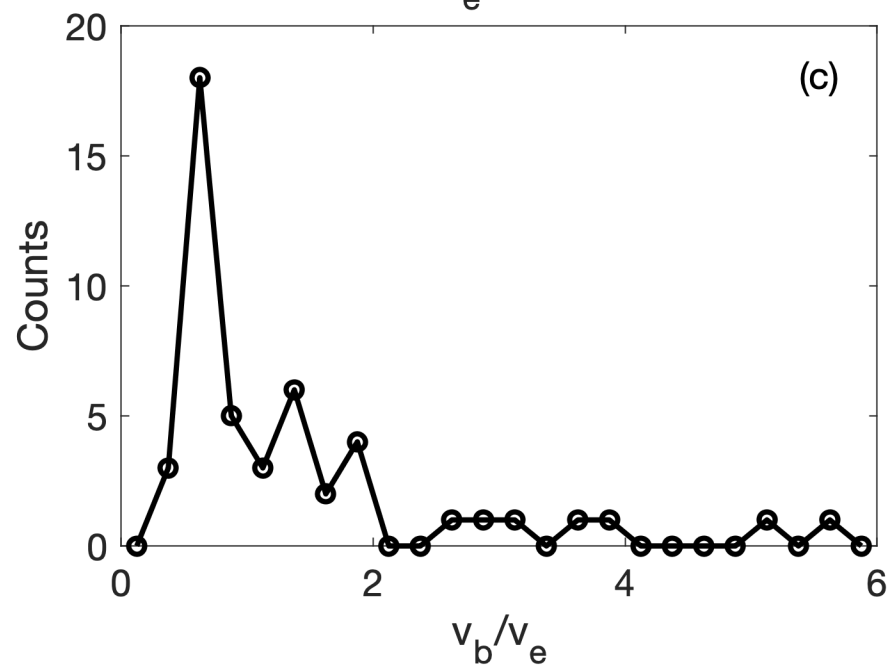
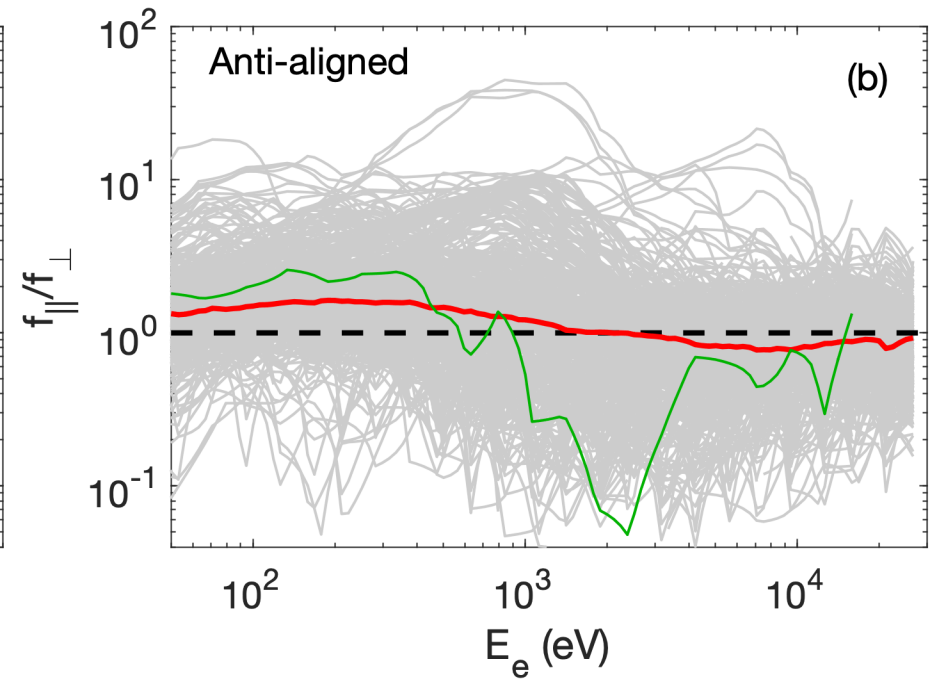
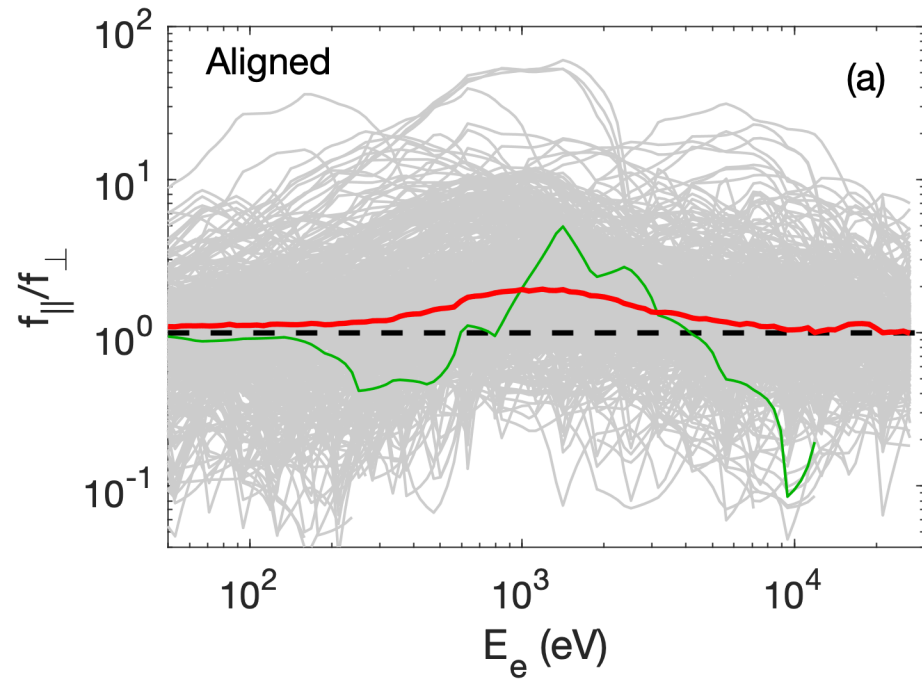


Figure 12.

MMS2

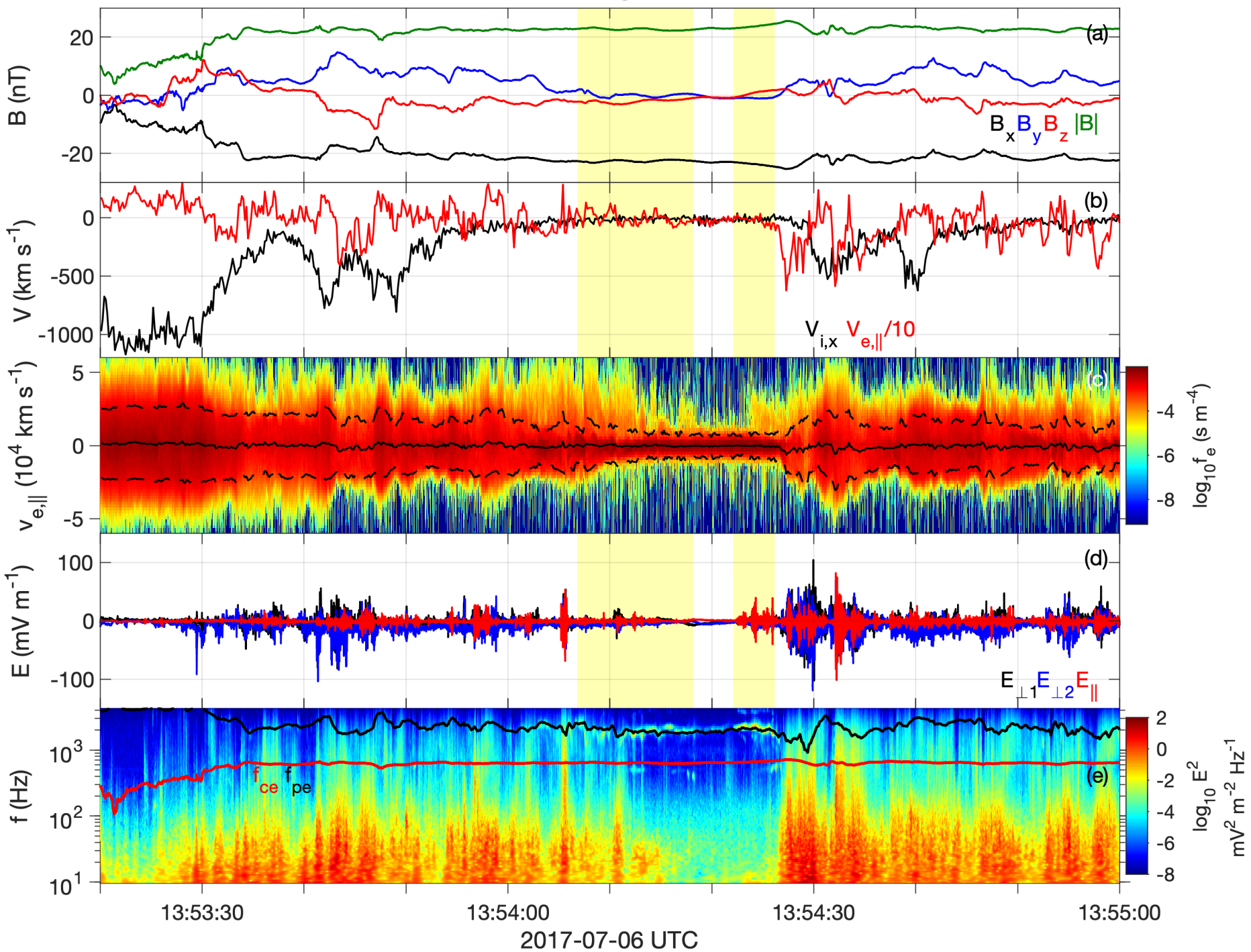


Figure 13.

MMS1

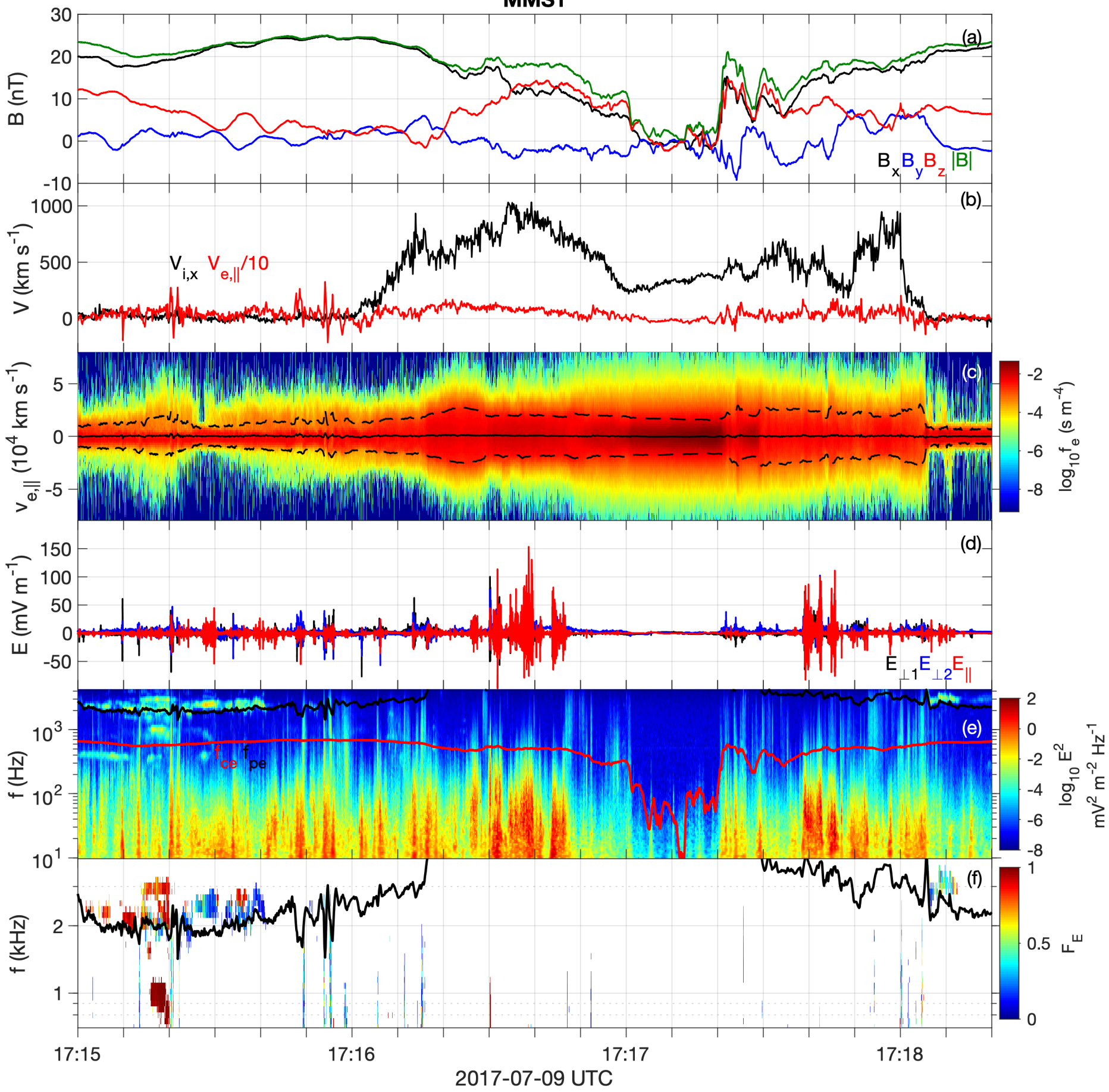


Figure 14.

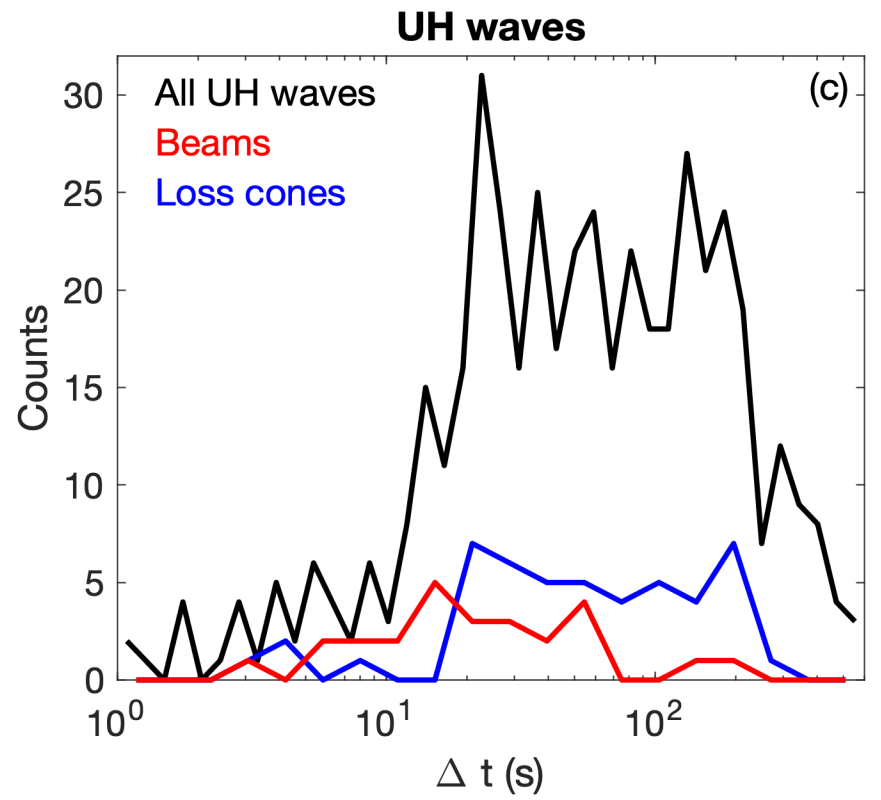
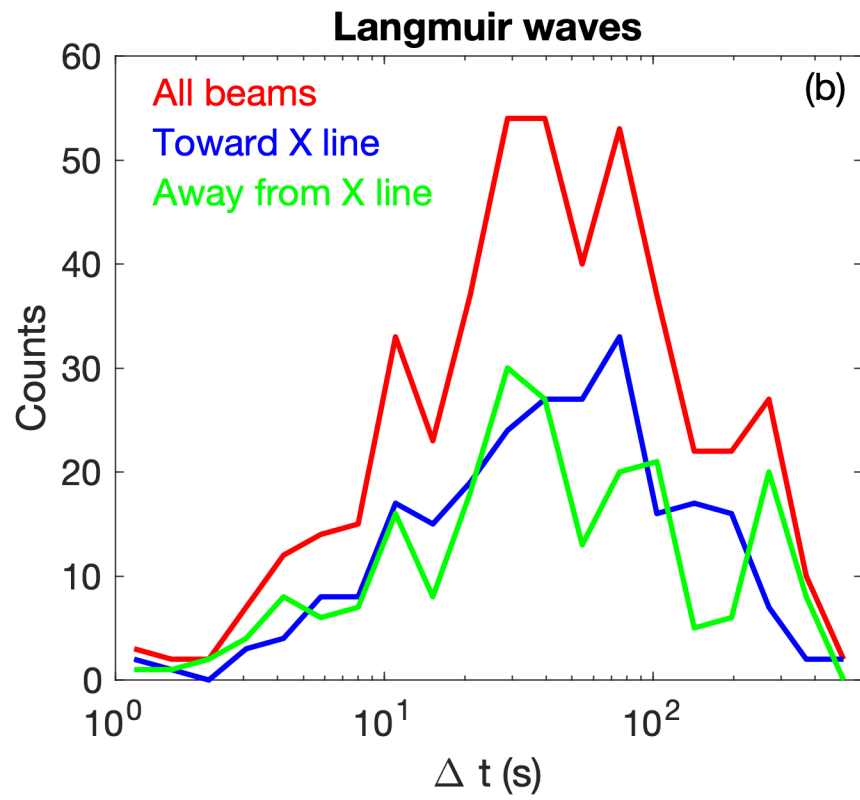
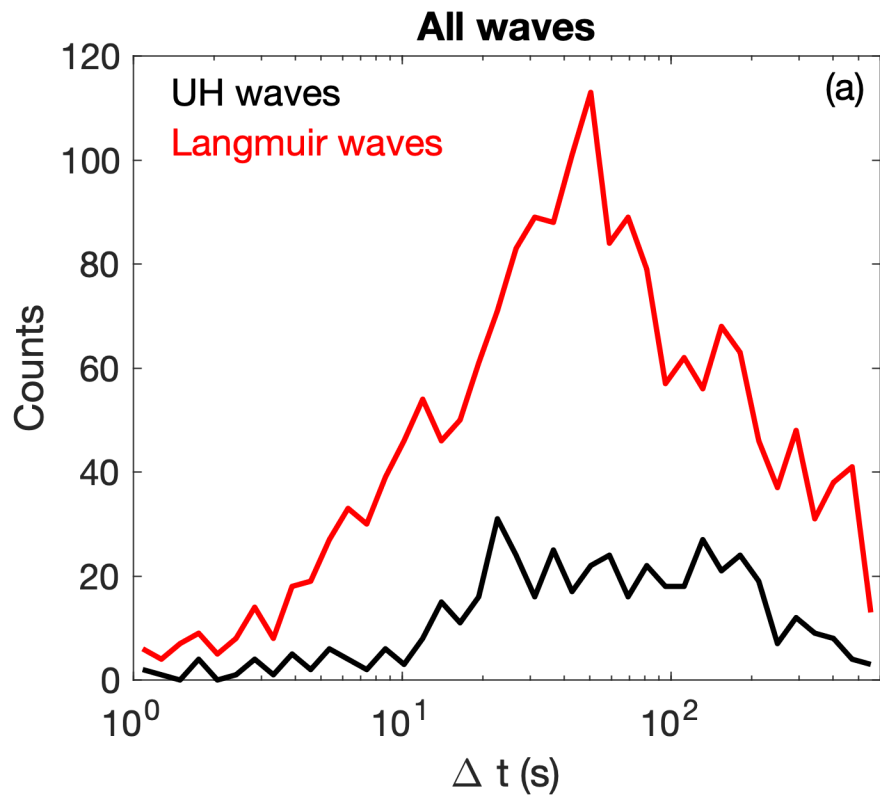


Figure 15.

